# Rays, Waves, and Separatrices

by

**Cristian R. Mendoza**

B.S., University of Colorado at Boulder, 2015

A thesis submitted to the

Faculty of the Graduate School of the

University of Colorado in partial fulfillment

of the requirements for the degree of

Master of Science

Department of Applied Mathematics

2015

This thesis entitled:
Rays, Waves, and Separatrices
written by Cristian R. Mendoza
has been approved for the Department of Applied Mathematics

Alan Mickelson

Prof. Gregory Beylkin

Prof. Mark Hoefer

Date

The final copy of this thesis has been examined by the signatories, and we find that both the content and the form meet acceptable presentation standards of scholarly work in the above mentioned discipline.

Mendoza, Cristian R. (M.S., Applied Mathematics)

Rays, Waves, and Separatrices

Thesis directed by Prof. Alan Mickelson

A qualitative study on the ray and wave dynamics of light in optical waveguides with separatrix geometry is presented herein. The thesis attempts to answer the question as to what happens in slab waveguides with a transverse refractive index distribution similar to the effective index distribution of a dual tapering waveguide. Discontinuous perturbations along the optical axis to the slab waveguide are also studied. A low-order method is used in this study. Light is found to be guided due to an interaction of the input signal with dynamical equilibria within the waveguide geometry. Dynamical systems and quantum separatrix crossing theory are utilized to explain paraxial propagation paths and modal power spectra of the segmented waveguide. Light confinement in the guide is reliant on the large number of degenerate higher-order modes present. Alternate solution methods are also discussed.

## Dedication

*Por mi familia y mi gente.*

## Acknowledgements

Thanks first off to my adviser, Dr. Alan Mickelson for advising this thesis. Through his guidance I have been able to learn much about one of my favorite topics—mathematical physics. I appreciate every conversation I have ever had with him. Furthermore, I would not have been able to study this year had it not been for this man, so a very special thanks goes out to Dr. Mickelson for facilitating my education and taking a chance on me.

My family has also been integral in my life and studies. Thanks to my mother, who has always encouraged me to dig deeper. Thanks to my sisters for dealing with excited rants about mathematics and education for the past five years. I hope that some of it left an impression on them.

I consider my friends to be an extension of my family, and if it were not for them, I may have lost my grounding at some point. Thanks to all of my friends, who have always encouraged me to stay honest.

Last but certainly not least, enourmous and very heartfelt thanks go out to Pieter Barker, Allyssa Riley, Gavin Medley, and Leland Giovannelli for lending a hand when I needed it the most.

# Contents

**Chapter**

# Figures

**Figure**

# Chapter 1

# Introduction

## 1.1 Statement of Purpose

This thesis attempts to showcase the qualitative relationship between two types of mathematical analyses. In particular, the treatment of light as a ray versus light as a wave is studied in the context of optical dielectric waveguides. These waveguides feature *separatrix geometry*, and exhibit interesting guiding qualities. Utilizing the relationship between the ray and wave picture of light in the context of nonlinear optics has recently attracted an effort from scientists in Europe (such as the investigations in [1], [2], [3], for example).

The Hamiltonian formalism of classical mechanics hinges on the characteristic function $H$. This formalism is easy to apply (in most cases) since the characteristic function of any physical dynamical system is the sum of the kinetic and potential energies associated with the system. Then the phase-space dynamics are given by partial derivatives of the characteristic function. A separatrix is formed in phase space whenever the potential energy has barriers (or wells) associated with it. A separatrix is a curve which divides phase space into different regions, and dynamics can be different in each of these regions. The separatrix is a *homoclinic orbit* of a dynamical flow, and it represents a barrier which cannot be crossed for autonomous systems. The classic example is the pendulum, whose angle from the vertical at a given time is governed by the second order differential equation

$$\ddot{\theta} + \frac{g}{l} \sin \theta = 0,$$

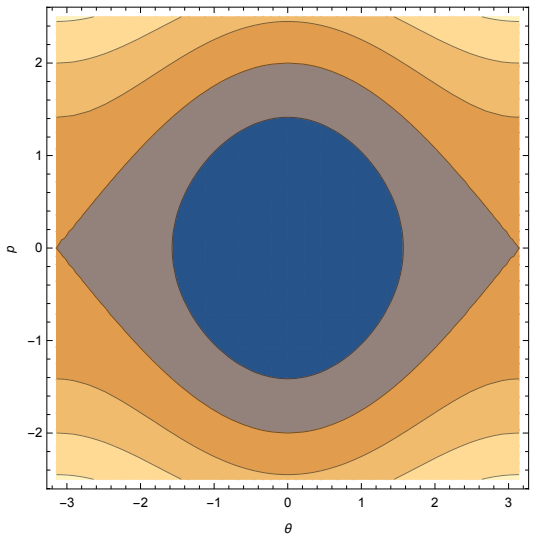


Figure 1.1: Phase space ($p$-$\theta$ space) for the pendulum. The separatrix is the eye-shaped border between the blue and orange regions.

where $g$ is the acceleration of gravity and $l$ is the length of the pendulum. Phase space for this differential equation is shown in figure (1.1).

The characteristic function (referred to as the Hamiltonian) for this system is

$$H(p,\theta) = \frac{p^2}{2} - mgl\cos\theta,$$

where $p = \dot{\theta}$ is the momentum of the pendulum. The variables $p$ and $\theta$ in this case define the dynamical phase space coordinates of the pendulum. In general, phase space is made up of *canonically conjugate* coordinates, usually defined to be a particle's position and its momentum. The separatrix is defined as the curve traced out in phase space when $H = mgl$. Orbits inside of the separatrix correspond to pendulum trajectories which swing back and forth in a periodic motion, while orbits outside of the separatrix are trajectories of the pendulum which go through full rotations [4]. When autonomous dynamical systems with separatrices undergo small, nonautonomous perturbations, interesting can dynamics arise. The stable and unstable manifolds between the separatrix have the potential to intersect, which can lead to erratic dynamical behavior. The intersection of manifolds is called a *homoclinic tangle*. In this case the separatrix no longer defines an "impenetrable boundary" in phase space. That is, the trajectories are allowed to undergo *separatrix crossing*.

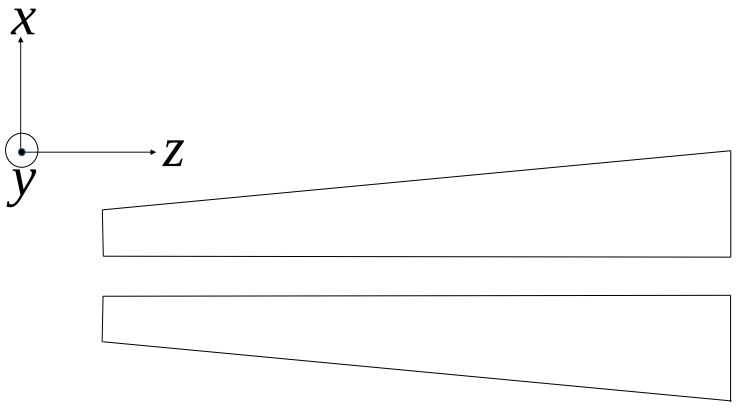


Figure 1.2: The dual tapering waveguide.

The discussion thus far has been classical. Separatrix crossing is also interesting to look at from a quantum mechanical point of view.

In the late eighties and early nineties, the theory of quantum separatrix crossing was developed. The punchline of the theory is that, for energy levels near the separatrix, eigenvalues of the Schrödinger equation become degenerate, and the adiabatic parameter begins to break down [5]. This means that the area traced out by a trajectory in phase space, which is the classical action of the system, is no longer conserved. This parameter is conserved elsewise.

The dual tapering waveguide (DTW) was invented in the Guided Wave Optics Laboratory in 1992 to study the quantum separatrix crossing theory outlined in [5]. The waveguide consists of two portions of material aligned symmetrically about the optical axis, $z$, whose widths slowly increase down the guide. A sketch of the waveguide is given in figure (1.2). Since the optical potential (which depends on the distribution of the refractive index of the guide) varies slowly in $z$ relative to its tranverse variance, the DTW is the "optical analog" to a slowly time-varying (with respect to its shape) potential in quantum mechanics. This is true since $z$ plays the role of the time variable in optics. Furthermore, in this formalism the amplitude of the electric (or magnetic) field plays the part of the electron wave function [6]. Hence, looking into the theory and implementation

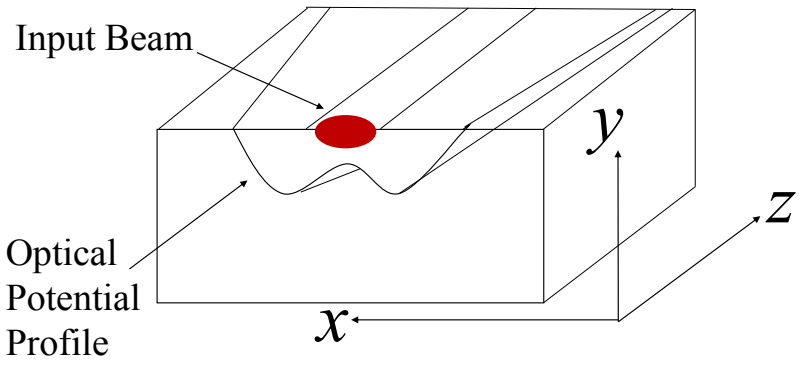


Figure 1.3: Experimental initial conditions for the DTW.

of optical waveguides serves as an extremely useful tool for studying quantum phenomena.

The DTW was theoretically and experimentally shown to exhibit properties predicted in [5]. Specifically, it was shown that, for a light signal incident above the separatrix (see figure (1.3)), it breaks into a large number of modes at the beginning of the waveguide. This means that the signal—which is due to an electromagnetic field—is decomposed into characteristic field distributions of the waveguide. This is the breakdown of the adiabatic parameter, since the area associated with a trajectory in phase space will be changing in $z$ due to the changing modes in that direction. The incident signal was taken from a single mode input (from an optical fiber) with a numerical aperture of less than .1. There was also an effort to attempt the focusing of a multimoded—that is, made of many modes—light spot such that the product $NA * A_{spot}$ is minimized, where $NA$ is the numerical aperture, and $A_{spot}$ is the area of incident light spot. The light at the end of the waveguide was seen to reside in both arms, having settled into a smaller number (1 to 2) of modes. This suggests that the dual tapering waveguide exhibits mode trapping [7], since light was present in both sections of the waveguide. The effective refractive index distribution of the dual tapering waveguide looks like a parabolic/gaussian distribution with an impression in the middle. This shape comes from the geometry of the DTW, since the refractive index inside the waveguide is higher than the surrounding material (this ensures guidance).

This thesis addresses the following questions:

- Qualitatively, what happens to the ray and wave dynamics of light in a slab waveguide which has a transverse index distribution similar to the dual tapering waveguide?
- What happens to the dynamics when the slab is subject to discontinuous periodic perturbations along the optical $z$ axis?

To study how the dynamics change due to the introduction of a separatrix, a refractive index distribution with a dynamical parameter which affects the creation or destruction of a separatrix in classical phase space will be used.

Waveguides with periodically discontinuous segments along the optical axis are called Periodically Segmented Waveguides (PSWs). Beam collimation in these types of guides has been investigated in [1]. Beams were collimated due to interactions with dynamically stable manifolds created by the geometry of the transverse refractive index distribution in the "high-index" region of the PSW. These waveguides have the property of frequency locking and mode filtering, which make them interesting candidates for theoretical analysis. The following describes the basics of the modes of analysis to be used in this thesis, along with a bit of contextual grounding.

## 1.2 Historical Background

Man's fascination with light is hardly a novel concept. This document begins with Fermat and Huygens, who both recognized that light could be treated as a ray or a wave. Fermat's idea is stated simply in what is now known as *Fermat's Principle*:

The path between two points taken by a ray of light leaves the optical length stationary under variations in a family of nearby paths [8].

One may recast the preceding statement as follows: a ray of light traveling from point $A$ to $A'$ does so in the least amount of time possible. For this reason, *Fermat's Principle* is also referred to as the *Principle of Least Time*. This hypothesis therefore defines the very notion of a ray of light, and

serves as the basis for what is known as Geometrical Optics. Huygens took an essentially reciprocal approach to that of Fermat. He suggested that light travels in "wave fronts", or phase fronts. The normal to these fronts correspond to the direction of travel and thus to Fermat's rays [9]. However, the construction of Huygens is geometrically sophisticated, and is difficult to comprehend when compared to the ray formalism. It may very well be for this reason that a corpuscular theory of light overtook the interest of the natural philosophers of the time. Among those philosophers one will find Sir Isaac Newton.

Newton's development of Calculus and a theory of gravity made his opinion holy to the British natural philosophy realm. He famously studied light and concluded that light was in fact a stream (or ray) of particles. Nearly a century later, polymath Thomas Young demonstrated the wave nature of light through his Double Slit Experiment. The year was 1802, and the result was not taken seriously, so Young decided to move onto Egyptology [10]. The end of the nineteenth century produced a mathematical formalism for an explanation of the Double Slit Experiment, although not for that specific end. The solution came in the form of Maxwell's Equations. These equations predicted that "light consists in the transverse undulations of the same medium which is the cause of electric and magnetic phenomena" [11], and also accounted for diffraction, interference, polarization, reflection, and refraction [12]. The phenomenon these equations could not predict, however, was the Photoelectric Effect.

The Photoelectric Effect is an observable natural phenomenon which occurs when light (at a specific frequency) incident on a metallic surface facilitates the liberation from that surface of what is called a "photoelectron". Note the dependence on *frequency*, as opposed to *amplitude*. Classical theory predicts that the liberation energy of the electron should be related to the intensity (and thus, the amplitude) of the incident light. This led Einstein to postulate that light travels in discrete energy quanta, and the development of quantum mechanics took place in an attempt to explain this occurence [12]. Thus the answer to the question of the nature of light was indeterminate: light behaves as both a particle and a wave. Indeed, this observation was extended to all matter (not just light) by DeBroglie in the 1920s.

The results of quantum mechanics eventually produced the laser in the late 50s/early 60s. The laser, though developed through quantum principles, produces lased photons. It is interesting to note that the existence of this light aligns more with Newton's concept of corpuscles than with a wave theory (of course, the quantum mechanical aspect of the laser is molecular). The 1960s saw the development of a theoretical framework such that effects such as second harmonic generation, stimulated Raman and Brillouin scattering, four-wave mixing, and intensity dependent refractive index could be explained [13]. It was soon thereafter that scientists began to pursue the idea of guiding such coherent light. The optical fiber was not an attractive choice initially, due to the high losses associated with silica glass. It was not until 1970 that a group of scientists at Corning were able to solve the loss problem by using fused silica and a cladding layer. This revolutionized the field of nonlinear optics and set into motion the development of these fibers for practical use [14].

## 1.3 Ground Work

Shortly after the cladding innovation, Dietrich Marcuse of Bell Laboratories published a now-seminal treatise on fiber optics and planar waveguides called *Theory of Dielectric Optical Waveguides*. The book features a rigorous application of wave theory to waveguides. The transcript begins with an analysis of planar asymmetric waveguides, and culminates in the presentation of the fabled coupled mode equations, and the associated coupled power equations which describe the propagation of light in a waveguide [15]. This system of coupled, ordinary differential equations which describes the relationship between the amplitudes of the forward propagating waves and the amplitudes of the backward propagating waves in the waveguide arises from a modal expansion of the electric field in the form (for x-polarization, for example):

$$E_x = \sum_{j=1}^{M} \left(b_j(z) + b_{-j}(z)\right) \Psi_j(x, y), \tag{1.1}$$

where $z$ is the direction of propagation, and $b_j$ and $b_{-j}$ correspond to the forward and backward amplitudes, respectively [6].

About ten years later, Allan Snyder and John Love released an exhaustive account of the theory which had developed over the last twenty years on the subject of light, fiber optics, and waveguides. This exposition also included then-novel approaches for the solution of standard problems in optics, including radiation losses via modal and Green's function methods, single mode/polarization fibers, crosstalk between fiber couplers, birefringence, a treatment of multi-mode fibers via geometrical optics, the so-called Gaussian approximation for fibers with circular and non-circular cross sections, and perturbation/asymptotic/variational methods as applied to the fiber optics field. The creation of this work is a reflection of Snyder's attitude toward optics: a fuller picture is offered by analyzing light as both a ray and a wave. The first part of the book concerns the ray theory of light, and walks through the mathematical structure of the theory, beginning at planar waveguides and building up to non-uniform fibers with bends. The section concludes with a discussion on diffraction. The second part is dedicated to the electromagnetic (i.e. wave) theory of light in the context of fibers. This part discusses the modes (bound and radiation) of an optical fiber and the coupling between them as predicted by Maxwell's Equations. The third part is an exposition of applications [6].

The book was published after nearly a decade of development in the field, of which Snyder was a part, along with a close collaborator Colin Pask. Pask was involved in some of the most fundamental results in the realm of fiber optics, such as the observation of rays in graded-index fibers [16]. He and Snyder developed a correction scheme for geometrical optics in the breakdown regime (the theory at the time suffered when applied to sufficiently long fibers) [17]. They also established the equivalence between Marcuse's statistical coupled mode theory and a theory arising from the notion of a plane wave in the geometrical optics limit [18]. Pask was also largely involved in the conversation of the relationship between chaotic phenomena and waves in fiber optics [19]. The tools cultivated and categorized by these scientists helped establish a solid foundation for the study of light in fiber optic waveguides.

The development of Periodically Segmented Waveguides (PSWs) primarily took place in the 1990s. Theory and fabrication met near the beginning of the millenium. In the middle of the last

decade, PSWs with interesting properties were theorized, and have since been shown (theoretically) to collimate light. If the simulations agree with experiment, PSWs may be very valuable for lasing and amplifying light.

## 1.4 Rays and Dynamics

A mathematically rigorous treatment of ray dynamics in optics is given in [8]. The argument is a variational one, aimed at minimizing the integral

$$\int_A^B n\left(\mathbf{r}(s)\right) ds, \tag{1.2}$$

which is the mathematical statement of the optical path length, as $n\left(\mathbf{r}(s)\right)$ is the refractive index distribution and $ds$ is an infinitesimal variation along the optical path. The minimization of this integral is equivalent to invoking Fermat's Principle. In general, it can be shown that the relationship which satisfies this hypothesis is given by the *ray equation* [20]:

$$\frac{d}{ds}\left(n\frac{d\mathbf{r}}{ds}\right) = \nabla n. \tag{1.3}$$

Remarkably, repeating the process of integral minimization for axial ray optics (where dynamics mostly take place near the optical axis) leads to the standard Euler-Lagrange differential equations (with the temporal dependence replaced with a dependence on the direction of propagation):

$$\partial_{\mathbf{q}} L = \frac{d}{dz}\partial_{\dot{\mathbf{q}}} L, \tag{1.4}$$

where the overdot denotes a derivative with respect to $z$, and $\mathbf{q}$ is the vector of transverse coordinates of the rays in a given coordinate system (Cartesian/polar). $\dot{\mathbf{q}}$ is the vector of slopes of the rays. Here, $L$ is the optical Lagrangian, and it is given by

$$L\left(\mathbf{q}, \dot{\mathbf{q}}, z\right) = n\left(\mathbf{q}, z\right)\sqrt{1 + |\dot{\mathbf{q}}|^2}, \tag{1.5}$$

$n(\mathbf{q}, z)$ is the refractive index distribution. Performing the standard Legendre Tranformation to the Lagrangian, one obtains the optical Hamiltonian:

$$H(\mathbf{q}, \mathbf{p}) = \mathbf{p} \cdot \dot{\mathbf{q}} - L(\mathbf{q}, \dot{\mathbf{q}}, z) = -\sqrt{n^2(\mathbf{q}, z) - |\mathbf{p}|^2}, \tag{1.6}$$

where $\mathbf{p}$ is the vector conjugate momenta of the components of $\mathbf{q}$ [8]. It should be noted here that the linearization of this Hamiltonian and the relationship between the analysis of light as a ray and the analysis of light as waves has been given a considerably wonderful formalism by Amalia Torre in [20].

The Hamiltonian formalism has been useful for dynamical analysis of optical waveguides. The Melnikov function, $M$, is defined as the distance between stable and unstable manifolds of a dynamical phase space. Melnikov's Theorem states that there exist homoclinic tangles in phase space if $M$ has zeros. The Melnikov function is given by

$$M(z_0) = \int_{-\infty}^{\infty} \{H_0, H_1\} \left( r^{(0)}(z), p_r^{(0)}(z), z + z_0 \right) dz, \tag{1.7}$$

where $H_0$ is an unperturbed Hamiltonian, taken to be the sum total of the potential and kinetic energies in a given system. $H_1$ is a sinusoidal term (in $z$) which we may append (after being multiplied by a small number $\epsilon$ such that $0 < \epsilon \ll 1$) onto the unperturbed Hamiltonian to study the effects on the dynamics of a system under a perturbation. Here, $r^{(0)}$ and $p_r^{(0)}$ are taken to be for a homoclinic orbit, and they represent the solutions of the Hamiltonian equations of motion in polar coordinates. $r$ is the radial distance from the optical axis and $p_r$ its respective momentum. The curly braces encompassing $H_0$ and $H_1$ denote a canonical Poisson Bracket between the two. In general—that is, in *any* coordinate system—this is given by

$$\{H_0, H_1\} = \sum_{i=1}^{n} \partial_{q_i} H_0 \partial_{p_i} H_1 - \partial_{p_i} H_0 \partial_{q_i} H_1, \tag{1.8}$$

where $n$ is taken to be the degrees of freedom of the system. The integral in the Melnikov function is taken over the homoclinic orbit, and $z_0$ is a phase delay. This has been utilized in showing the existence of homoclinic tangles in optical fibers [21].

A simple, one-dimensional development of an equation of motion for a ray is given by Ajoy

Ghatak in his book *Optics*, and is repeated here. Consider a one-dimensional ray of light propagating in the $z$-direction, with the optical path length given by $s$. Consider further a small snippet of the path $ds$. Refer to figure (1.4). Denote the *invariant* of the path by $\gamma$ such that $\gamma = n(x_0)\cos\theta_0$,

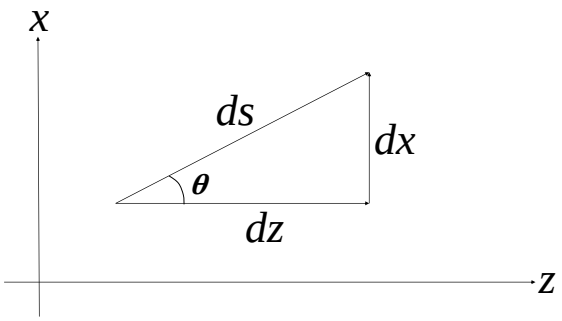


Figure 1.4: The setup for the derivation of the one-dimensional equation of motion of a ray of light.

where $x_0$ and $\theta_0$ are reference data. Then, by the Pythagorean Theorem (and dividing through by $dz$), it is plain to see that

$$\left(\frac{ds}{dz}\right)^2 = \left(\frac{dx}{dz}\right)^2 + 1. \tag{1.9}$$

Referring further to the figure, it is apparent that $\cos\theta = \frac{dz}{ds}$. Then

$$\left(\frac{1}{\cos\theta}\right)^2 = \left(\frac{ds}{dz}\right)^2 = \frac{n^2(x)}{\gamma^2}. \tag{1.10}$$

Plugging this into eq.(1.9) and differentiating both sides with respect to $z$ yields the equation we seek:

$$\ddot{x} = \frac{1}{2\gamma^2}\frac{dn^2(x)}{dx}, \tag{1.11}$$

where again the overdot denotes a derivative with respect to $z$ [22]. This will be the dynamical equation used in the classical approach of the thesis.

To facilitate a Hamiltonian analysis, we re-write the previous equation as a system of first order differential equations. The optical conjugate momenta (i.e., the slope of a ray) is given by

$$\mathbf{p} = \partial_{\dot{\mathbf{q}}} L = \frac{n(\mathbf{q})\dot{\mathbf{q}}}{\sqrt{1+|\dot{\mathbf{q}}|^2}} = n(\mathbf{q})\sin\theta, \tag{1.12}$$

where $\theta$ is the angle between the ray and the optical axis. In paraxial ray optics, the small-angle approximation is used to set $\dot{x} = \theta$ [23]. The one-dimensional paraxial Hamiltonian may then be written as

$$H(\theta, x; \gamma) = \frac{\theta^2}{2} - \frac{1}{2\gamma^2} n^2(x), \tag{1.13}$$

so that the equations of motion in phase space are given by

$$\begin{aligned} \dot{x} &= \partial_\theta H = \theta, \\ \dot{\theta} &= -\partial_x H = \frac{1}{2\gamma^2} \frac{dn^2(x)}{dx}. \end{aligned} \tag{1.14}$$

These equations form the basis of the ray analysis to follow.

## 1.5 Maxwell's Equations and the Parabolic Wave Equation

The pertinent equations in this treatment of light are Maxwell's Equations:

$$\begin{aligned} \nabla \times \vec{E} &= -\partial_t \vec{B}, \\ \nabla \times \vec{H} &= \vec{J} + \partial_t \vec{D}, \\ \nabla \cdot \vec{D} &= \rho, \\ \nabla \cdot \vec{B} &= 0, \end{aligned} \tag{1.15}$$

where $\vec{E}$ is the electric field, $\vec{H}$ is the magnetic field, $\vec{D}$ is the electric displacement vector, $\vec{B}$ is the magnetic flux density, $\vec{J}$ is the current density, and $\rho$ is the volumetric charge density. If we assume $\vec{J} = \vec{0}$, $\rho = 0$, along with harmonic time dependence of the electric field (that is, $\vec{E} \propto e^{-i\omega t}$) and ignore the nonlinear polarization term produced from taking the curl of the curl of this field, Maxwell's Equations reduce to the Helmholtz Equation for $\vec{E}$:

$$\nabla^2 \vec{E}(\mathbf{r}) + k^2(\mathbf{r}) \vec{E}(\mathbf{r}) = 0, \tag{1.16}$$

where $k^2(\mathbf{r}) = k_0^2 n^2(\mathbf{r})$, and $k_0^2 = (\frac{\omega}{c})^2$. Suppose now that the electric field takes the form

$$\vec{E}(\mathbf{r}, t) = \mathbf{Re}\left\{ \psi(\mathbf{r}_t, z) e^{-i(kz + \omega t)} \right\} \vec{\mathbf{e}}_p. \tag{1.17}$$

Here $\mathbf{r}_t$ is the vector of transverse components, $k = k_0 n_0$, and $\vec{\mathbf{e}}_p$ is a polarization vector, taken to be for a transverse magnetic (TM) mode. Then it is noted that

$$\partial_z^2 \vec{E} = \mathbf{Re}\left\{\left(\partial_z^2\psi - 2ik\partial_z\psi - k^2\psi\right)e^{-i(kz+\omega t)}\right\}\vec{\mathbf{e}}_p. \tag{1.18}$$

The Paraxial Assumption is now envoked. That is, it is assumed that $|\partial_z^2\psi| \ll |2k\partial_z\psi|$ [23]. Once this ansatz for the electric field is inserted into the Helmholtz Equation (1.16), and the harmonic dependence on time and the axial $z$ coordinate is divided out of all terms (since all terms share it and it will never be zero), one finds

$$\nabla_t^2\psi - 2ik\partial_z\psi + k_0^2(n^2(\mathbf{r}) - n_0^2)\psi = 0. \tag{1.19}$$

Rearranging this equation:

$$\frac{i}{k_0}\partial_z\psi = \frac{1}{2n_0}\left(\frac{\nabla_t^2\psi}{k_0^2} + n^2(\mathbf{r}) - n_0^2\right)\psi. \tag{1.20}$$

Let

$$H_{opt} = \frac{1}{2n_0}\left(\frac{\nabla_t^2}{k_0^2} + n^2(\mathbf{r}) - n_0^2\right), \tag{1.21}$$

so that we may write

$$\frac{i}{k_0}\partial_z\psi = H_{opt}\psi. \tag{1.22}$$

This is the parabolic wave equation. This equation is to serve as the governing equation in the wave approach of this thesis. Note that the optical Hamiltonian operator here is not necessarily Hamiltonian in the definitional sense. That is, this operator may not have any definiteness associated with it, and thus it would not conserve the systems' energy (as Hamiltonians are known for doing). In other words, the optical Hamiltonian has scattering programmed into it via the optical potential term, which we denote as

$$V_{opt} = \frac{n^2(\mathbf{r}) - n_0^2}{2n_0}. \tag{1.23}$$

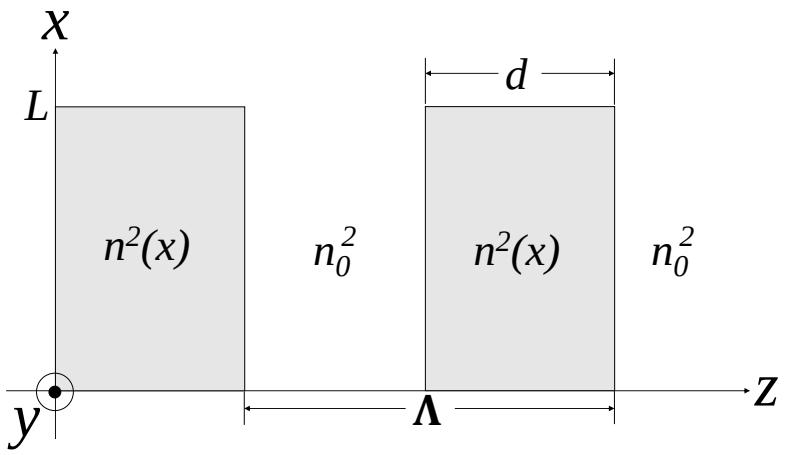


Figure 1.5: The Periodically Segmented Waveguide in a constant $y$-plane.

## 1.6 Periodically Segmented Waveguides

Consider the following situation. Let the direction of propagation of a light signal be given by $z$. Suppose the configuration of interest is such that there is no variation in the transverse direction $y$. Now let the transverse component about which the refractive index in the high regions shall vary be denoted by $x$. Suppose segments of high index (constant or variable) with length $d$ and width $L$ are placed periodically along the $z$-axis with period $\Lambda$. The regions between these segments, as well as the surrounding material, have a constant index $n_0$ associated with them. In this setup, the optical axis is located at $z = L/2$. The described configuration is given in figure (1.5).

The *Duty Cycle* of a PSW is given by the ratio of the length of the high-index regions to the segmentation period: $DC = d/\Lambda$. With this information, it can be seen [1] that the refractive index distribution in the $p$th segment ($p = 1, 2, ...$) of the PSW can be written as

$$n^2_{PSW}(x,z) = \begin{cases} n^2(x); & (p-1)\,\Lambda \le z \le (DC+p-1)\,\Lambda \\ n_0^2; & (DC+p-1)\,\Lambda < z < p\Lambda. \end{cases}$$

The theory and eventual fabrication of the PSW developed mainly during the 1990's. Lithium Niobate in-diffused with Titanium (Ti:$LiNbO_3$) was among the forerunners for the compound of

choice for engineering these guides [24]. The first full-modal analysis of the PSW was provided in [25]. The distribution in the high segments was taken to be constant and close ($\delta n = .015$) to that in the low index regions. It was concluded that the effective index difference ($\Delta n'$) in the PSW was proportional to a comparable uniform waveguide, with the duty cycle being the constant of proportionality between the two. Properties concerning the loss factor $\alpha$ were also surmised based on this analysis. It was observed that $\alpha$ monotonically increased with increasing $\Delta n'$, but that it oscillates with the segmentation period, duty cycle, and also with the wavelength of light used in the waveguide. Some results even show $\alpha$ zero-ing out for some configuration of the waveguide. This phenomenon was explained (via the calculations in the paper) to be caused by an interaction with the guided and radiated modes of the PSW. Another interesting result from this investigation: since most of the loss curves for the second order mode had peaks where the loss curves of the fundamental modes had valleys, one could take advantage of this to perform mode filtering. The analysis used a Fast-Fourier-Transform (FFT) Beam-Propagation-Method (BPM) for their 2D calculations, and had planned to use a Finite-Difference (FD) BPM for 3D calculations. The authors predicted the use of PSWs for 2D mode tapers, asymmetric couplers, and asymmetric wavelength splitters. An experiment performed on a PSW made of Ti:$LiNbO_3$ (which had similar parameters to those in the modal study) confirms all of the properties observed in the theoretical exposition. However, special consideration was given to the loss in the waveguide associated with the concentration of in-diffused Ti, and it was found that the surface loss is more prominent for short periods and the segmentation loss takes over for longer periods. It was also seen that, for decreasing duty cycle, the width of the mode decreased, but it was independent of the segmentation period [24]. The main problem with these waveguides was a material one. Due to photorefractive damage induced by high power densities within the guide, there exists a relative instability of this material at the visible and near infrared wavelength. A group out of the National Institute of Standards and Technology (NIST) applied a layer of neodymium (Nd) to continuous slab waveguides made of Ti:$LiNbO_3$ to produce double-moded waveguides in the infrared (800-1040nm) with coupling efficiency of $\sim 68\%$. The Nd quells the photorefractive damage and leads to efficient lasing, with the output power about

70% of the input power [26]. This is an interesting fabrication consideration.

A ray analysis via Gaussian Matrix ray tracing is used to analyze the PSW in [27]. This analysis applies strictly to multimode structures, and with it there was shown to exist stable and unstable regions of the PSW such that rays launched passed a certain angle of incidence ($\theta_{max}$) escape the waveguide. This angle was found to vary with the duty cycle and the segmentation period. Again, applications for input/output coupling in the field of integrated optics are speculated on the basis of mode size transformation (that is, an amplitudinal tapering of modes) observed for certain configurations. The authors end with a discussion of using the ray equation to the same ends. One year later, the properties of PSWs mentioned above were, for literally the first time, observed in [28], using a technique referred to as "fluorescent visualization". A popular convention in all of these results were to compare to an analagous continuous waveguide (CWG) for verification. The ability to do this was not present in 2006, when a group a scientists used a Gaussian distribution in the high-index regions.

The numerical analysis (based on the 1D ray equation previously derived) of the PSW with Gaussian disribution high-index segments involves a nonlinear equation which exhibits resonances which play a part in ray divergence (or guidance). These resonances manifest themselves in what is known as frequency locking. This effect is not present in a continuous waveguide with a Gaussian index distribution. Frequency locking only happens when the ratio of some short period along the ray path with the segmentation period is a rational number. A stunning picture of the dynamics is visualized with the help of a Poincaré Section, which shows stochastic regions intertwined with resonance islands separated by KAM tori. These tori serve as barriers which cannot be crossed by a ray trajectory, and thus it is concluded that the stability of the nonlinear resonances depends on the ray's intial condition (i.e. if it were within a torus). This serves to make the propagation of resonances "more robust with respect to external perturbations" [29]. The treatment is extended in [30], where the dispersion properties of the rays in a Gaussian PSW (GPSW) are studied. It is found that the transit time (the time it takes to get from one side of the waveguide to the other) between rays in the GPSW and a comparable CWG were in agreement if the ray in the GPSW

was launched on/near a resonance. An antisymmetric Gaussian distribution is also considered, and in both cases it is shown that the ray dispersion (corresponding to the loss factor $\alpha$) is not monotonic with $\Delta n'$, and that the transit time increased with decreasing index difference, which seems non-intuitive. The reason a serious analogy between a GPSW and a CGW could not have been drawn was because of the absence of a complicated topology in phase space in the case of a CGW. In [31], a Frequency-Domain (FreqD) BPM is used on the paraxial parabolic wave equation. In a recent paper by the same group, these results are used to calculate a *Husimi Distribution*, the contour plot of which is a wave-dynamical analog to classical phase space. The modal power spectrum of the PSW for varying cases of waveguide parameters is also calculated. The spectrum is given by the Fourier Transform of the cross-correlation integral between the amplitude of the input signal with the amplitude of the electric field within the waveguide [1]. Finite Element (FE) techniques have been applied to this problem in [32] and [33].

## 1.7 Biomedical Applications of PSWs

This section briefly discusses the application of PSWs in the context of biosensing. The interaction of the guided modes of the PSW with its radiation modes is utilized in the design of interferometry-based optical sensors, which measure changes in refractive index. This produces sensors with high sensitivity but low quality factor. In the passed decade, the utility of PSWs as biosensors has been investigated as a label-free-alternative to the prevalent "tagging" method. These devices belong to a larger class of silicon photonic biosensing devices, and there exist advantages and disadvantages to using PSWs when compared to other designs.

The most widely used biosensors rely on a technique known as "tagging". The method involves depositing a known substance onto an analyte (such as RNA or DNA, for example) and monitoring the resulting electrochemical reaction through some measuring process. The most common measuring process is that of flourescence, in that the biosensor will measure the amount of flourescent light from a reaction between the tagging material (pre-manipulated to include the

flourescent material) and an analyte. There also exist methods which immobilize antibodies and other molecules to measure an analyte [34].

These devices are mostly fabricated in glass, silicon, and polymers. However, the design of any device is not unique. In 2004, a silicon waveguide tagging biosensor with a nanocavity was fabricated with a quality factor of 182.3. The sensor used a micron-sized planar silicon photonic device to detect ultralow concentrations of metal nanoparticles. The quality factor is the ratio of the energy in the device to the energy lost. When the nanocavity diameters were only slightly varied, the spectrum of the device shifted dramatically. As a consequence, a signal can be strongly trapped within the small region of the waveguide.

The applications of these sensors are rather mainstream, such as medical diagnostics. However, their use requires a trained professional and can be costly. The cost comes from the fabrication of these devices [35]. The ability to obtain fast results from these sensors is also limited. To address these issues, label-free, optical biosensors have been investigated and fabricated.

Much like their labeling counterparts, the design of label-free biosensors is also non-unique. Many designs have been explored. For example, microcantilever beams have been employed as a label-free biosensor. This device measures changes in mass by sensing deflections of the cantilever. This has proven to be useful in eliminating the need for tagging. However, the measurement nevertheless requires isolation of the vibration of the cantilever, and has the added requirement of needing the probe molecules to be bound to the surface of the beam [36]. Optical devices offer an alternative which allows for even less interaction with the biomaterial.

Other designs which have been implemented include TE/TM mode microring resonators, as well as disk resonators. These types of devices exhibit a high quality factor. A property these sensors share with thin waveguide resonators is that they exhibit enhanced interaction with the evanescent fields assocatiated with them. This aspect makes these sensors attractive since the evanescent fields of biomaterial are the fields one would hope to measure with these devices. A device which exhibits high $Q$ (in exchange for sensitivity) is a sensor with a waveguide designed as a Bragg grating [35]. Biosensensors with PSWs are particularly sensitive to interactions with

evanescent fields. These types of sensors use interferometry to measure a refractive index changes in biomaterial. Of the many flavors of interferometry, Mach-Zehnder and Fabry-Perot interferometry have been used in designing sensors integrated with PSWs.

Mach-Zehnder interferometry involves splitting a light beam into two parts and reconstructing them back into one signal. This type of interferometry measures interference by division of amplitude. The beam is split by the aplty-named beam splitter, which is simply a piece of glass with dielectric or metal coating on the front surface [37]. Amplitude-based interferometry is conjugate to the (more popular) type which measures intereference by means of a phase change. The Fabry-Perot interferometer is of this flavor.

A Fabry-Perot interferometer consists of closely spaced, partially silvered surfaces. A lens is sometimes used to focus the output into concentric circles on a screen to visualize the phase splitting. Incoming light is reflected on the surfaces multiple times, and a portion of the signal is transmitted each time the light reaches the end of the array. This interaction results in multiple offset beams which interfere with each other to produce a high resolution image [38]. The integration of these interferometers into a biosensor is nontrivial, but is accomplished with the use of PSWs.

Optical biosensors are attractive since they are not affected by mechanical forces, fluid flow, or electromagnetic interference. The integration of a PSW into biosensing systems give the system a high degree of sensitivity, due to the aforementioned properties of these waveguides. These types of sensors are used for *bulk sensing* (as opposed to surface sensing). The use of optical sensing is known as a differential method, since only *differences* in the refractive index can be measured. This differs from direct methods, for example, which measure the true index. Properties vary between Fabry-Perot and Mach-Zehnder configurations.

The PSW-Mach-Zehnder Interferometry (PSW-MZI) biosensor consists of two arms (a reference and a sensor) which have PSWs integrated along them. It has a sensing length of about .24mm, and can measure changes in refractive index on the order of $3.96\times10^{-5}$ (when there are 48 cycles in the PSW). This device has a theoretical signal-to-noise-ratio (SNR) of about 50dB [39].

On the other hand, the Fabry-Perot PSW biosensor, also known as a 1-D photonic band gap structure, can measure refractive index changes as small as $4\times10^{-5}$. However, this device manages to do this with an SNR of 29dB and a sensing length of 720$\mu$m [40]. In this sensor, only one of the arms has a PSW along it.

Another configuration of PSWs in biosensing to periodically segment a ring resonator. This produces tunable modal overlap with the analyte due to weak mode confinement. Thus this configuration is ultra-sensitive to interactions with evanescent fields. The SNR of this setup is 60dB, and a $Q$ of 3,898. To reach the theoretical sensitivity limit, the $Q$ would need to be closer to 15,000. If the segmentation period is much less than the ratio of the half the wavelength to the effective index, then a lossless mode is supported in the PSW [35]. These properties are interesting, but the PSW biosensor also exhibits a few drawbacks.

The main drawback of the PSW biosensor is the low quality factor $Q$. Due to this, the sensing limit of the microring resonator PSW biosensor is about 3 times away from the theoretical limit. There is also a mode mismatch at the interface of the waveguide and the ring. Furthermore, other devices (such as the previously mentioned thin waveguide resonators and Bragg gratings) are easier to manufacture because of industry standards. There is also a current lack of compatability with unprocessed clinical samples, so the actual use of these devices remains elusive. Secondary amplification is still needed to achieve low enough sensitivies for this application. This is another aspect curtailing the actual use of these sensors. In terms of a design criticism, the surface of the chip could be affected by interactions with proteins, thus degrading the chips sensitivity [35]. Despite these few drawbacks, a look toward the future application of PSW biosensors (and optical sensors in general) can nevertheless be speculated upon.

The application of optical biosensors would be for medical diagnosis. If developed to the point of applicability, these devices have the potential to replace tagging biosensors, which are the most widely used in the healthcare industry in this day and age. These sensors would get rid of the need for a trained professional to spend hours on making a measurement, thus reducing the cost of diagnostic healthcare. The results from these devices are delivered much quicker. The

most prevalent type of diagnostics is called Point of Care (POC) diagnostics, and this includes diagnosing pregnancy and measuring blood sugar. Sixty to seventy percent of all healthcare decisions are impacted by POC diagnostics. These devices can also be used to diagnose infectious diseases and perform blood typing analysis. Thus optical biosensors might be part of the answer to affordable/sustainable healthcare [35].

## 1.8 Outline of Thesis

The main focus of this thesis is the application of the means of analysis presented in the literature review to investigating the ray and wave dynamics of light in slab waveguides and PSWs. The transverse refractive index of these waveguides is to feature a dynamical parameter which will affect the creation or destruction of a separatrix in classical phase space because of the shape of the optical potential. In particular, we take a look at four values of this parameter. The geometry of phase space for two of these values features a double-well separatrix. The reason these cases are of interest is because they resemble the effective refractive index of the DTW. Special attention is paid to using the results of the ray analysis to inform (initial) conditions on the wave analysis. Results of both analyses are then used, along with Quantum Separatrix crossing theory, to arrive at the anticlimactic conclusion that waveguides featuring separatrix geometry are interesting theoretical tools which deserve a more rigorous investigation.

In chapter two, the symmetric slab waveguide is studied. Ray paths and paraxial wave propagation are presented which show guidance properties of the waveguide. To motivate the study of PSWs, homoclinic tangles are shown to exist within the waveguide under continuous periodic perturbations along the optical axis. In the wave picture, modal power spectra are calculated to conceptualize the number of modes in, and their contributions to, the optical power in the slab.

Chapter three presents simulation results for the PSW. Light is seen to behave erratically but is still guided for some configurations. Stroboscopic plots are used to visualize the topology of the phase space associated with this type of waveguide. Paraxial propagation of the electric field down the waveguide is presented, along with a calculation of the modal power spectrum. Results

show an extremely large amount of degenerate modes within the PSW.

The final chapter concerns alternative solution methods for the equation of motion in the wave case, both analytic and numeric. Then conclusions about the dynamics of light in waveguides studied herein are discussed. The thesis ends by mentioning considerations for future work.

# Chapter 2

# Continuous Waveguides

In this chapter, the analysis of a continuous slab waveguide with a particular refractive index distribution is presented. A dynamical ray analysis is performed via a Hamiltonian formalism. The response of the waveguide to periodic perturbations along the direction of propagation is investigated. The impetus behind this investigation is given by the inherently periodic nature about the z-axis of PSWs. Then, a wave approach via Maxwell's equations is presented. A Fourier expansion method is used to solve the resulting parabolic wave equation. In the paraxial realm, the calculated solution to the Schrödinger-Like-Equation (SLE) for the amplitude of the electric field inside of the waveguide as it propagates along the z-direction is presented. Then the modal power spectrum of the waveguide is calculated and presented. Results show a large multimoded-ness of the slab, as well as degeneracies of the higher-order modes.

## 2.1 Setup

A slab waveguide consists of a region of high index (possibly variable) placed in between two layers of constant index. The outer layers have lower refractive index than the inner, to ensure guidance along the middle of the waveguide. The slab is called asymmetric if the indeces of the outer layers are not equal to each other. Here we take the slab to be symmetric. That is, $n_0^2 = n_2^2$, where the subscript denotes the layers of the waveguide, indexed from 0. We further take the index in the high region to be variable along the transverse directions to that of propagation ($x$ and $y$ in

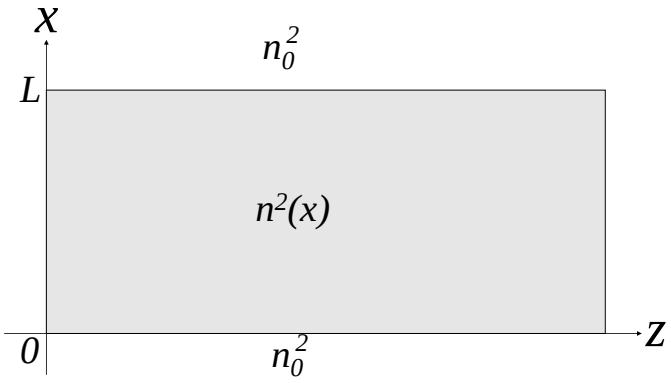


Figure 2.1: The Symmetric Planar Slab Waveguide.

Cartesian coordinates). If $x$ and $y$ are the transverse components, then $z$ is the component parallel to the direction of propagation. We will restrict our attention to the case where the waveguide is uniform in $y$. Thus the problem becomes two-dimensional, and the distribution of the refractive index in the core of the guide is given by $n^2(x)$. A picture of the described situation is given in figure (2.1).

We now turn our attention to finding a distribution of refractive index in the high region to use in this study. The domain for $n^2(x)$ is $x \in [0, L]$. We seek a distribution which looks like

$$n^2(x) = n_0^2 + \delta n \eta(x), \tag{2.1}$$

where $\delta n = \frac{n_1 - n_0}{n_1}$, and $n_1 = 2.15$ and $n_0 = 2.11$ are the guiding and substrate indeces, respectively. In the spirit of previous research, namely [1], $\eta(x)$ is taken to be a linear combination of Gaussians. In this thesis, the Gaussians are symmetric about $x = 1$ (so that $L$=2 in numerical simulations):

$$\eta(x; \mu_{1,2}, \sigma_{1,2}) = n_1^2 \left( \exp\left( -\frac{(x - (1 + \mu_1))^2}{2\sigma_1^2} \right) + \exp\left( -\frac{(x - (1 - \mu_2))^2}{2\sigma_2^2} \right) \right). \tag{2.2}$$

For the sake of simplicity, we take $\sigma_1 = \sigma_2$ (equal to .2 in numerical simulations), and we further take $\mu_2 = -\mu_1$, so that $\eta(x)$ now takes the form

$$\eta(x; \mu, \sigma) = n_1^2 \left( \exp\left( -\frac{(x - (1 + \mu))^2}{2\sigma^2} \right) + \exp\left( -\frac{(x - (1 - \mu))^2}{2\sigma^2} \right) \right). \tag{2.3}$$

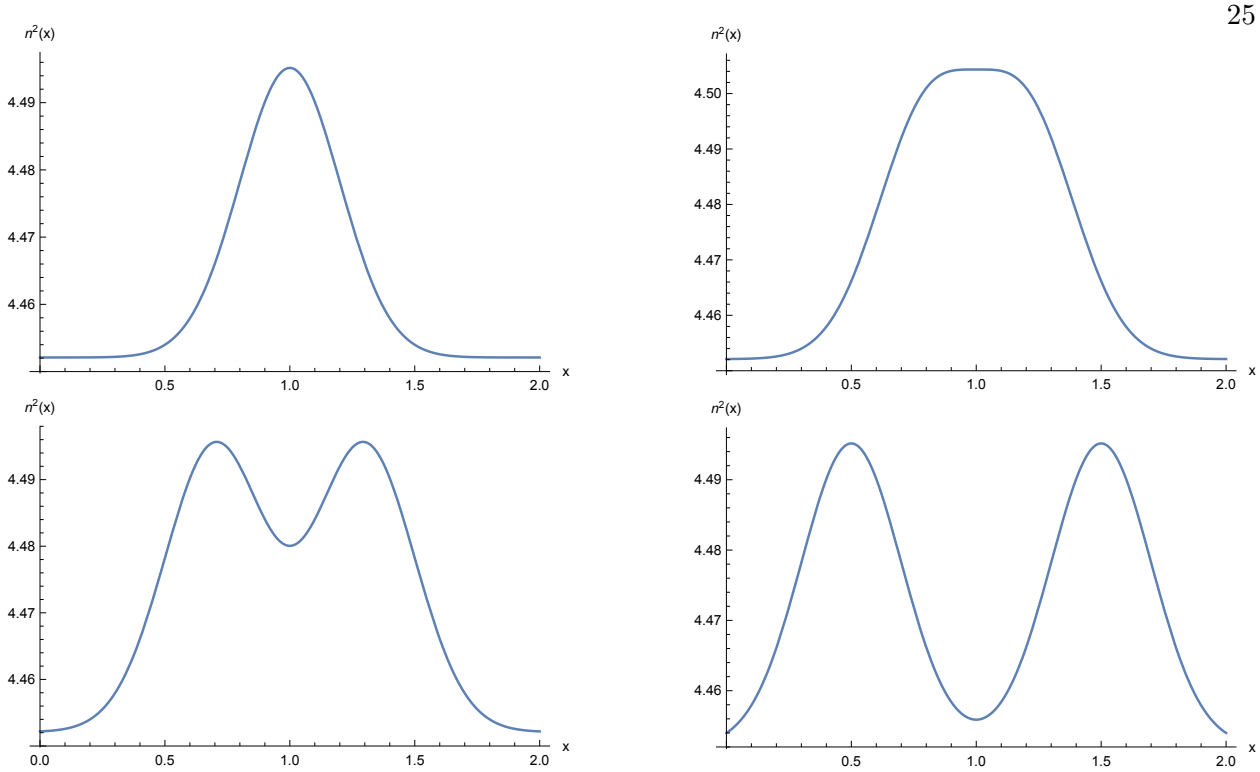


Figure 2.2: $n^2(x;\mu,\sigma)$ as a function of $x$ for $\mu$= 0, .2, .3, and .5 (going left to right, row by row). $\sigma$ is taken to be .2, and L=2. The range of this function is $[n_0^2, n_0^2 + \delta n n_1^2]$.

$n^2(x;\mu,\sigma)$ for the cases where $\mu$=0,.2,.3, and .5 is plotted in figure (2.2). These will be the four values we follow to study how the dynamics change as a separatrix is introduced.

## 2.2 Ray Analysis

The propagation of a ray of light in the planar slab waveguide in two dimensions is given by the second-order differential equation

$$\ddot{x} = \frac{1}{2\gamma^2}\frac{dn^2(x)}{dx}, \tag{2.4}$$

where $\gamma = n(x_0)\cos\theta_0$ is the invariant of the path for initial postion $x_0$ and angle $\theta_0$ [22]. The paraxial Hamiltonian $H(\theta, x)$ is given by

$$H(\theta, x;\gamma) = \frac{\theta^2}{2} - \frac{1}{2\gamma^2}n^2(x). \tag{2.5}$$

Having defined the Hamiltonian, the equations of motion for a ray of light in phase space are given by

$$\dot{x} = \partial_\theta H = \theta, \tag{2.6}$$

and

$$\dot{\theta} = -\partial_x H = \frac{1}{2\gamma^2}\frac{dn^2(x)}{dx}. \tag{2.7}$$

Contour plots of the Hamiltonian for the four values of $\mu$ discussed in the last figure and for $x_0 = .5$, $\theta_0 = \frac{\pi}{16}$ are given in figure (2.3). A dynamical systems analysis of this Hamiltonian system is now presented. The case where $L = 2$ and $\sigma = .2$ is specifically considered.

### 2.2.1 Dynamics

Since the system of interest is Hamiltonian, it may be written as

$$\dot{\vec{u}} = J\nabla H, \tag{2.8}$$

where $\vec{u} = (x, \theta)^T$, and $J$ is the *Poisson matrix* [4]:

$$J = \begin{pmatrix} 0 & 1 \\ -1 & 0 \end{pmatrix} \tag{2.9}$$

Thus finding the equilibria of this system amounts to finding the critical points of the Hamiltonian $H$. Since $\dot{x} = \theta$, then $\theta = 0$ is the $\theta$-critical point of this system. If $\mu = 0$, then $x = 1$ is the only $x$-critical point. Elsewise, the $x$-critical points are given by $x = 1, 1 \pm \mu$. To classify these equilbria, we linearize about each of them. Let any equilbria be denoted by $u^* = (x^*, \theta^*)$, and let the vector of points near this equilibrium be given by

$$\delta\vec{u} = (x - x^*, \theta - \theta^*)^T. \tag{2.10}$$

Then the equations of motion obeyed by $\delta\vec{u}$ may be written as

$$\delta\dot{\vec{u}} = JS\delta\vec{u}, \tag{2.11}$$

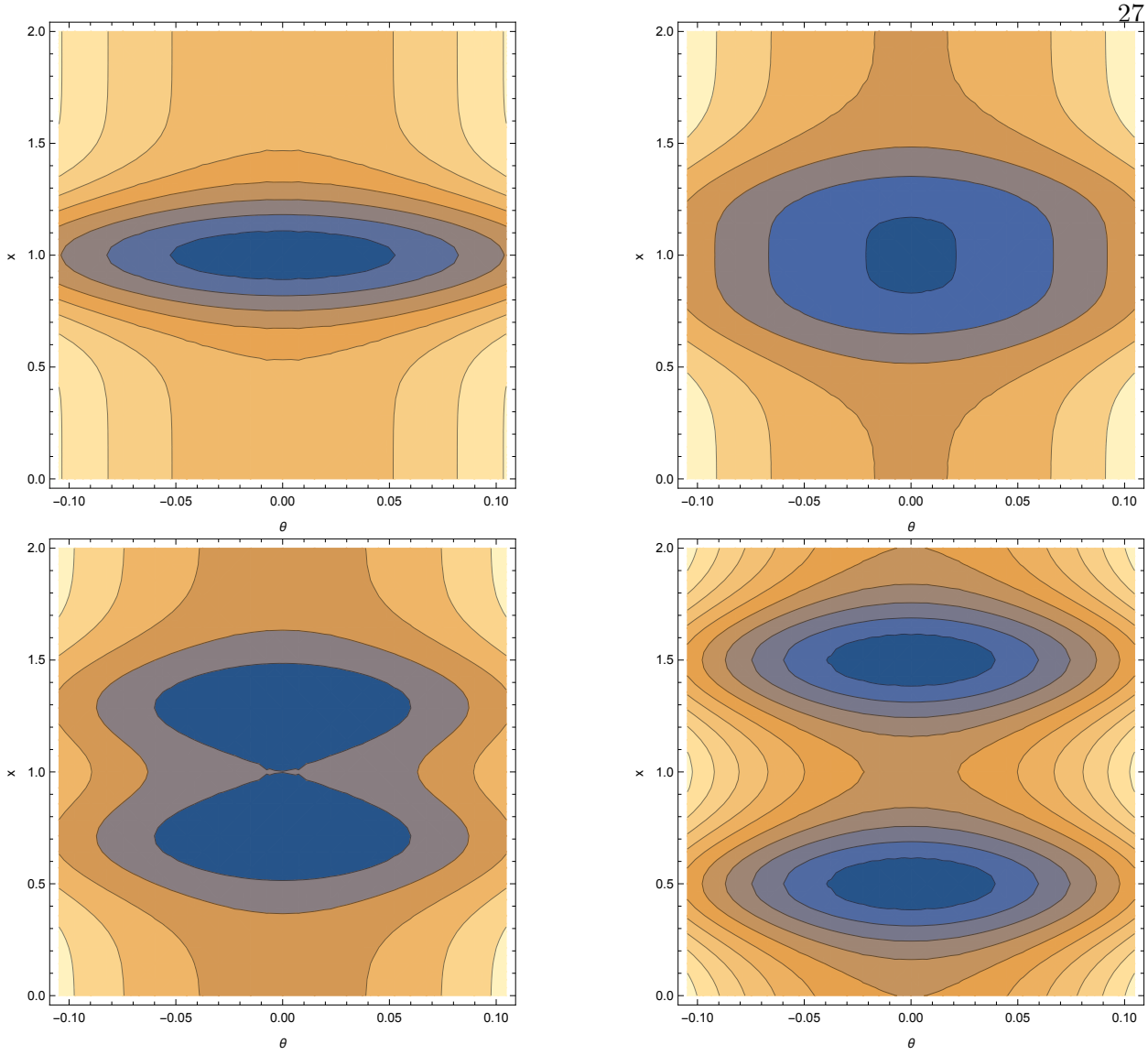


Figure 2.3: Contour plots of the Hamiltonian as a function of $\theta$ and $x$ for $\mu$= 0, .2, .3, and .5 (going left to right, row by row). Here, $x_0 = .5$, and $\theta_0 = \frac{\pi}{16}$.

where $S = Hes(H(u^*))$ is the Hessian matrix of the Hamiltonian evaluated at the equilibrium $u^*$. The matrix $K = JS$ forms what is known as a *Hamiltonian matrix*. The eigenvalues of $K$ are related to stability properties of $u^*$. In particular, if the eigenvalues of $K$ at $u^*$ are degenerate zero values (which will always come in pairs of two), then $u^*$ is a parabolic equilibrium point. If the eigenvalues are purely imaginary, then $u^*$ is a center, and is an elliptic equilibrium point [4]. In the

present case, the Hamiltonian matrix looks like

$$K = \begin{pmatrix} 0 & \partial_\theta^2 H(u^*) \\ -\partial_x^2 H(u^*) & 0 \end{pmatrix}.$$

The characteristic polynomial of this matrix is

$$p_K(\lambda) = \lambda^2 + \partial_\theta^2 H(u^*)\partial_x^2 H(u^*). \tag{2.12}$$

Here we see that, if the product $\partial_\theta^2 H(u^*)\partial_x^2 H(u^*)$ is real, then the eigenvalues of $K$ are purely imaginary. This is the case for non-zero $\mu$ at $x^* = 1 \pm \mu$, since the second derivative of the Gaussians will be real at these points. At $x^*$=1, the eigenvalues of the Hamiltonian matrix are both equal to zero, which makes this point a parabolic equilibrium point. This means that this point changes from an elliptic (center) point when $\mu$=0 to a hyperbolic (saddle) point if $\mu \neq 0$. This constitutes a pitchfork bifurcation which arises from the creation of a separatrix in phase space. The creation of a separatrix as $\mu$ changes can be seen from the contour plots in figure (2.3). Figure (2.4) shows the ray paths along the waveguide for different values of $\mu$.

### 2.2.2 Continuous, Periodic Axial Perturbations

We consider now Hamiltonians which have the form

$$H(\theta, x, z) = H_0(\theta, x) + \epsilon H_1(x, z), \tag{2.13}$$

where $H_0$ is the unperturbed Hamiltonian:

$$H_0(\theta, x) = \frac{\theta^2}{2} - \frac{1}{2\gamma^2} n^2(x), \tag{2.14}$$

and $H_1$ looks like

$$H_1(x, z) = A\frac{x^2}{2}\sin(\nu z). \tag{2.15}$$

Here $\epsilon$ is taken to be small ($0 < \epsilon \ll 1$). Furthermore, $A$ is some amplitude, and $\nu$ is the frequency of perturbation. To understand what the addition of this term does to the dynamics in the waveguide, the method of Melnikov is applied. The Melnikov function, $M$, is defined as the distance between

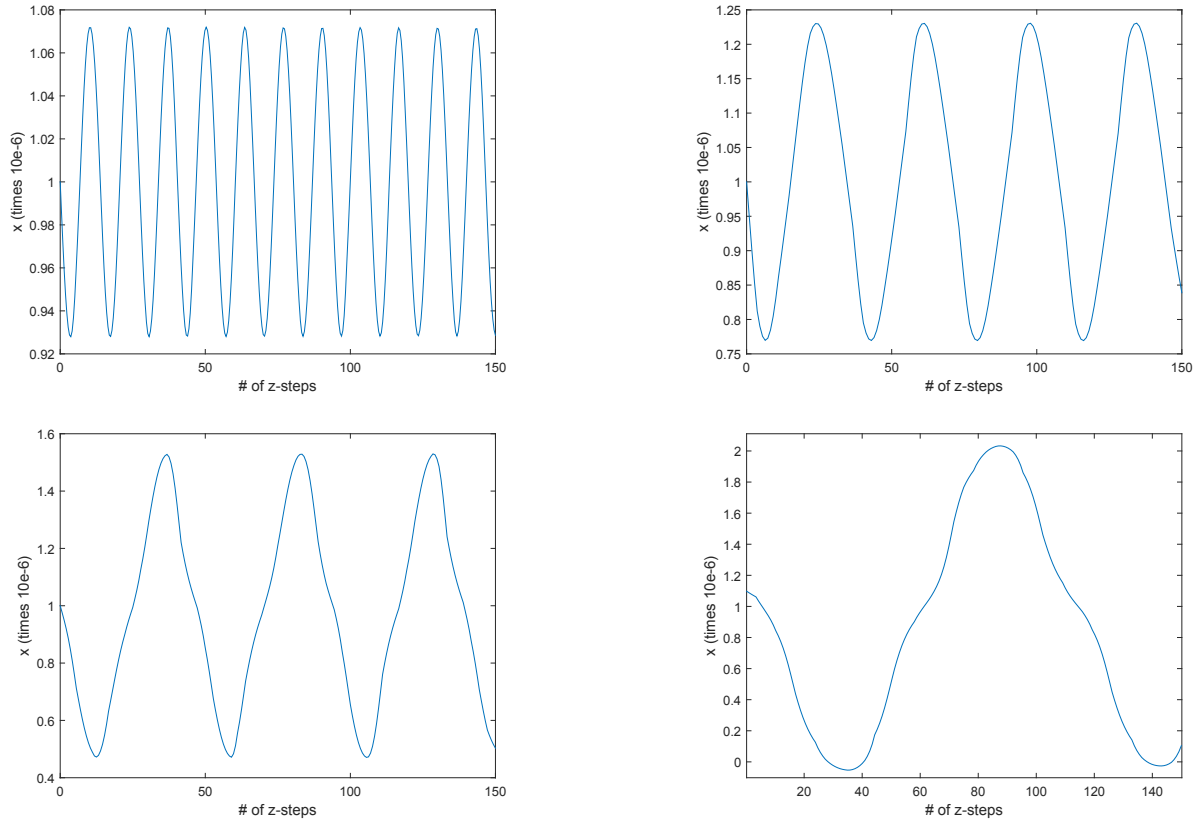


Figure 2.4: Plots of the ray paths in the waveguide for $\mu$= 0, .2, .3, and .5 (going left to right, row by row). Here, $x_0 = 1$, and $\theta_0 = -\frac{\pi}{90}$. $x_0$=1.1 when $\mu$=.5 since the saddle equilibrium point prohibited guidance.

stable and unstable manifolds of a dynamical phase space. Melnikov's Theorem states that, for small enough perturbations, there exist homoclinic tangles in phase space if $M$ has zeros.The Melnikov function is given by

$$M(z_0) = \int_{-\infty}^{\infty} \{H_0, H_1\} \left(\theta^{(0)}(z), x^{(0)}(z), z + z_0\right) dz, \tag{2.16}$$

Here $x^{(0)}$ and $\theta^{(0)}$ are taken for a homoclinic orbit. The curly braces encompassing $H_0$ and $H_1$ denote a canonical Poisson Bracket between the two. The integral is taken over the homoclinic orbit, and $z_0$ is a phase delay [21]. To apply this theorem, we first calculate the Poisson Bracket

between the two Hamiltonians:

$$\begin{aligned}\{H_0, H_1\} &= \partial_x H_0 \partial_\theta H_1 - \partial_\theta H_0 \partial_x H_1 \\ &= -Ax\theta \sin(\nu z)\,.\end{aligned} \tag{2.17}$$

Melnikov's function becomes

$$\begin{aligned}M(z_0) &= -\int_{-\infty}^{\infty} Ax^{(0)}(z)\theta^{(0)}(z)\sin(\nu(z+z_0))\,dz, \\ &= -A\sin(\nu z_0)\int_{-\infty}^{\infty} x^{(0)}(z)\theta^{(0)}(z)\cos(\nu(z))\,dz,\end{aligned} \tag{2.18}$$

after the application of the sum-to-product identities and noting that the product $x^{(0)}(z)\theta^{(0)}(z)$ is even since both of the functions in the product are even themselves. This is apparent from the symmetry of the contours of the unperturbed Hamiltonian. Then the integral will evaluate to some value, call it $\Xi$. Thus the Melnikov function is

$$M(z_0) = -A\Xi\sin(\nu z_0). \tag{2.19}$$

At this point it is clear that the Melnikov function zeros out for $z_0 = \frac{n\pi}{\nu}$, for $n \in \mathbb{Z}$. Thus there exists an infinity of transverse intersections of the stable and unstable manifolds in phase space. This means that a homoclinic tangle takes place within the waveguide under continuous, periodic axial perturbations. A plot of trajectories of light in phase space for $\mu$=.3 under this perturbation is given in figure (2.5). Hence we should expect interesting dynamics under a discontinuous perturbation.

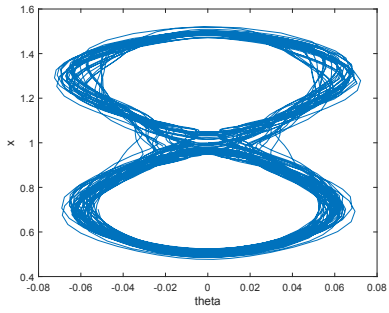


Figure 2.5: Trajectories in phase space under an axial perturbation in the waveguide for $\mu$= .3, showing a homoclinic tangle. The tangle is characterized by the fact that the ray does not trace out a constant contour in phase space. Here, $x_0 = .7$, and $\theta_0 = -\frac{\pi}{60}$.

## 2.3 Wave Analysis

Here we are concerned with the solution of the parabolic wave equation which was derived in the introduction:

$$\frac{i}{k_0}\partial_z\psi = H_{opt}\psi. \tag{2.20}$$

Recall,

$$H_{opt} = \frac{\nabla_t^2}{2n_0k_0^2} + V_{opt}(x),$$

where

$$V_{opt}(x) = \frac{n^2(x) - n_0^2}{2n_0}$$

is the optical potential. This equation shall be solved subject to zero Dirichlet boundary condtions and some initial profile $\psi(x, z = 0) = \psi_0(x)$.

### 2.3.1 Solution Method

It is well-known that the solution of the SLE can be expressed as a linear combination of the eigenvectors of $H_{opt}$:

$$\psi(x, z) = \sum_{n=0}^{\infty} \xi_n(z)\phi_n(x), \tag{2.21}$$

where $\xi_n(z) = \langle\phi_n(x), \psi(x, z)\rangle$. The eigenvectors are determined by the eigenvalue equation:

$$H_{opt}\phi_n = \varepsilon_n\phi_n, \tag{2.22}$$

where $\varepsilon_n$ is the $n^{th}$ eigenvalue. We now take the inner product of the $n^{th}$ eigenvector of $H_{opt}$ with the SLE:

$$\langle\phi_n(x), \partial_z\psi\rangle = \langle\phi_n(x), -ik_0H_{opt}\psi\rangle. \tag{2.23}$$

Now, using the definition of $\xi_n(z)$ along with the fact that $H_{opt}$ is Hermitian, we obtain an ODE for $\xi_n(z)$:

$$\xi_n'(z) = -ik_0\varepsilon_n\xi_n(z). \tag{2.24}$$

Given $\psi_0(x)$, the solution to equation (2.24) is

$$\xi_n(z) = \xi_0 e^{-ik_0\varepsilon_n z}, \tag{2.25}$$

where $\xi_0 = \langle \phi_n(x), \psi_0(x) \rangle$. Thus the solution to the SLE may be expressed as

$$\psi(x,z) = \sum_{n=0}^{\infty} \langle \phi_n(x), \psi_0(x) \rangle \phi_n(x) e^{-ik_0\varepsilon_n z}. \tag{2.26}$$

### 2.3.2 Numerical Implementation

The Dirichlet boundary conditions in this case call for a generalized Fourier sine series solution to satisfy equation (2.20), hence we define the inner product between two functions $f(x)$ and $g(x)$ on the interval $x \in [0, L]$ as

$$\langle f(x), g(x) \rangle = \frac{2}{L} \int_0^L f(x) g(x) dx, \tag{2.27}$$

which is the $L^2$ inner product on $[0, L]$. The inner product which concerns us is $\langle \phi_n(x), \psi_0(x) \rangle$. To find $\phi_n(x)$, we use Finite Differences to discretize $H_{opt}$ into a matrix $\mathbf{H}$:

$$(\mathbf{H}\psi)_{i,j} = \left( -\frac{1}{h^2 n_0 k_0^2} + V_{opt}(x_j) \right) \psi_j + \frac{1}{2h^2 n_0 k_0^2} \left( \psi_{j-1} + \psi_{j+1} \right). \tag{2.28}$$

where $h = \frac{L}{N}$. Alternatively, we may express $\mathbf{H}$ in matrix form (on a grid of $j$ points $x_j = jh$ ($j =$ 1, 2, 3,...,$N-1$)):

$$\mathbf{H} = \begin{pmatrix} -\frac{1}{h^2 n_0 k_0^2} + V_{opt}(x_1) & \frac{1}{2h^2 n_0 k_0^2} & & 0 \\ \frac{1}{2h^2 n_0 k_0^2} & \ddots & \ddots & \\ & \ddots & \ddots & \frac{1}{2h^2 n_0 k_0^2} \\ 0 & & \frac{1}{2h^2 n_0 k_0^2} & -\frac{1}{h^2 n_0 k_0^2} + V_{opt}(x_{N-1}) \end{pmatrix}$$

$\mathbf{H}$ is symmetric and real, thus it is Hermitian. Now that the discrete operator $\mathbf{H}$ has been found, the discretized $\phi_n(x)$ are computed using a canned eigenvector solver. Once we have the eigenvectors, the inner product between them and the initial condition is performed using the composite Simpson's Rule.

The next step towards finding the solution is to construct the two-dimensional arrays $\psi_n(x, z)$. This is done by simply evaluating the complex exponential term on the z-grid then storing columns of x-data, each multiplied by a z-value, into an array. The number of z-points was taken to be equal to the number of x-points, $N$. These values were set to be 512 in simulations. The final step is to sum all of the $N$-1 arrays.

#### 2.3.2.1 Accuracy

There are three sources of error in this approach. The first is truncation error in the solution. However, since the Fourier coefficients can be made to decay arbitrarily quickly as $n \to \infty$ (depending on the smoothness of the initial condition), other error sources will be the culprit of inaccuracy. The other source of error is due to discretization. That is, the usage of Finite Differences to discretize the optical Hamiltonian, and the composite Simpson's Rule to discretize the $L^2$ inner product will be the cause of inaccuracy of this method. Specifically, since a technique is only as accurate as its least accurate component (this is not true for iterative schemes), we expect no better than second-order accuracy in the calculations obtained via this solution method. That is to say, the usage of FD has second-order error, which is the lowest order of accuracy between itself, truncation, and the composite Simpson's Rule (which has fifth-order error associated with it) [41].

### 2.3.3 Results

A magnitude-normalized Gaussian Beam was used as the input profile for $\psi_0(x)$. Initial conditions were set such that $\theta_0 = 0°$ and $x_0 = x^*$, with a width of $\sigma_{in} = .02$. That is,

$$\psi_0(x) = \exp\left(-\frac{(x - x^*)^2}{2\sigma_{in}^2}\right). \tag{2.29}$$

The input wavelength was taken to be $\lambda_0$ =1.55$\mu$m, and solutions were constructed from $z = 0$ to $z$=6mm. Paraxial propagation of the beam down the slab is shown in figure 2.6. The most striking property of these plots is the periodic structure of the beam. This structure is referred to as "snake-

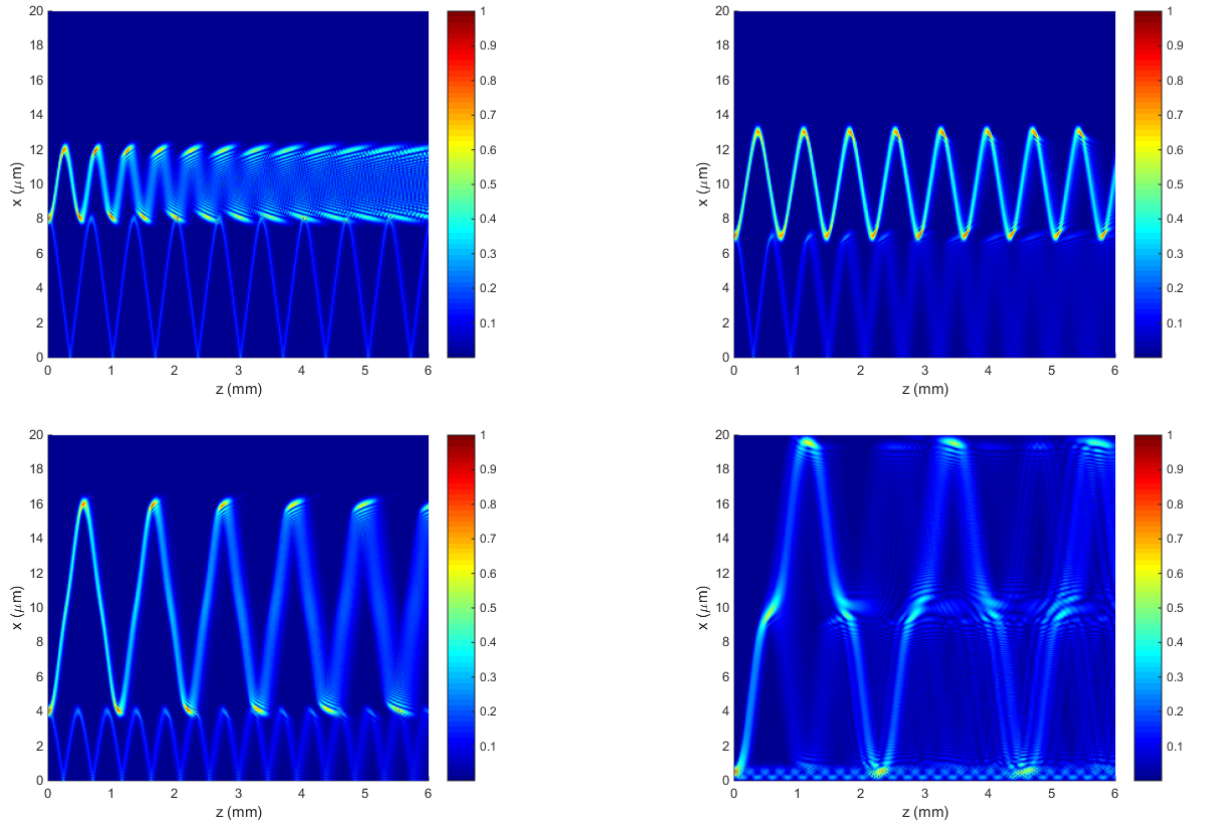


Figure 2.6: Contour plots of normalized $|\vec{E}(x,z)|$ for $\mu$= 0, .2, .3, and .5 (going left to right, row by row). The input valuess were chosen such that the initial conditions were just outside of an equilibrium point. Artifacts are due to the Dirichlet boundary conditions at $x$=0 and $x = L$.

like collimation" in [1]. The reason behind this shape is the interaction of the magnitude of the $E$-field with the optical potential. Initial conditions were chosen to be just outside of the equilibria points, to fascilitate transverse oscillation of the signal across the waveguide. Initial conditions too close to an equilibrium oscillated aboiut that point, and initial conditions *at* the equilibria traveled in a straight line down the waveguide.

To further confirm the multimoded-ness of the slab, the number of modes within the waveguide is given by

$$V = k_0 \rho n_{co} \sqrt{2\Delta}, \tag{2.30}$$

where $\rho$ is the radius of the waveguide, $n_{co}$ is the base refractive index in the guiding region (or "core" in the case of a fiber), and $\Delta = \delta n$ [6]. In the present case, we have that

$$V = \frac{\pi L}{\lambda_0}\sqrt{2n_1\,(n_1 - n_0)}.$$

$$\sim 2.70562\ e6.$$

An idea of how the power in a waveguide is distributed about the modes present within it can be found via an algorithm proposed by Feit and Fleck in [42]. The basic version of this algorithm is to calculate the cross-correlation integral between $\psi_0(x)$ and $\psi(x, z)$:

$$K(z) = \int_0^L \psi_0^*(x)\psi(x, z)dx,$$

where the asterisk denotes the complex conjugate. We then multiply $K(z)$ by a Hanning window function $w(z) = 1 - \cos\left(\frac{2\pi z}{z_f}\right)$, where $z_f$ is the length of the waveguide. This is done to help filter noise in the signal. The modal power spectrum is then the Fourier Transform of this product:

$$T(\beta) = \int_0^{z_f} K(z)w(z)e^{i\beta z}dz.$$

Plots of the magnitude of the modal power spectra for the slab are given in figure (2.7).
The initial conditions in figure (2.7) were chosen to be the same as the those in figure (2.6). One can see from the plots that there seem to be many near-degenerate modes supported by the guide. These plots confirm not only the multimoded-ness of the slab, but also that most of the power in the slab is within the higher-order modes. The thick regions of the spectrum coincide to a low variation of the group delay $\partial_\omega \beta_n$ (for the $n^{th}$ $\beta$), which means that there are large mode group velocities associated with these regions of the spectrum. The group velocity is defined as the inverse of the group delay, which is a measure of phase distortion of the waveguide [42].

It should be noted that the algorithm given in [42] is slightly more sophisticated than what was done here. We have skipped over the interpolation step due to the theoretical nature of of this analysis. That is, these results are within an order of magnitude to those in [42], and since the solution method is first order, it suffices to investigate a more efficient solution method for the

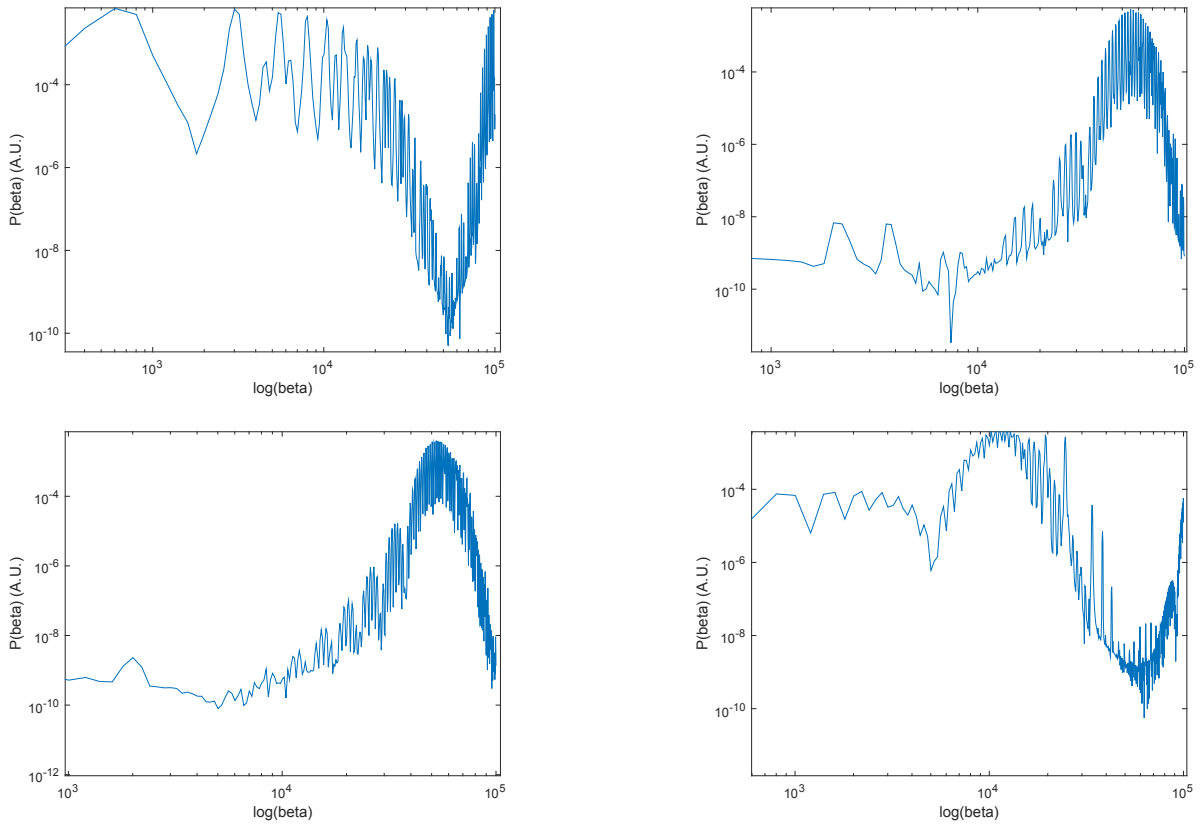


Figure 2.7: Plots of $|T(\beta)|$, the modal power spectrum, for $\mu$= 0, .2, .3, and .5 (going left to right, row by row). Simulations were performed with $N$=512 points.

PDE before working too heavily with the data it outputs. Considerations of alternate methods are discussed in Chapter 4. The next step to see how this guide responds to a discontinuous perturbation.

# Chapter 3

# Periodically Segmented Waveguides

In this chapter we present the results of numerical experiments modeling the dynamics of light in a Periodically Segmented Waveguide. Ray paths and stroboscopic plots of the dynamical phase space are presented. After discussion of the solution to the parabolic wave equation in the low-index regions, the paraxial propagation of a Gaussian beam down the waveguide is presented. Light behaved in a somewhat predictable fashion, but the trajectories were markebly different for differing initial conditions. The calculated modal power spectrum indicates a degeneracy of the higher order modes, and that there is noticable power contained within some of them due to this fact.

## 3.1 The Problem at Hand

We now look at the case of a discontinuous periodic axial perturbation to the slab wave guide. Let the regions of the PSW occupied by a section of material which has variable index $n^2(x)$ be known henceforth as the high-index regions. The constant-index portions between the high-index regions are then the low-index regions. For a given length $d$ of the high-index region, the main parameters we shall concern ourselves with are the segmentation period $\Lambda$, and the *duty cycle* ($DC = d/\Lambda$), along with the four values of $\mu$ which we have been following. Specifically, we present results for $\Lambda$ =2$\mu$m. Differing values of the Duty Cycle were chosen based on the half- or full-period of oscillation of the electric field amplitude within the slab equivalent. They were chosen such that the interface between the low- and high-index regions was at these periods to propagate

the signal through when it is its most intense. The value of $\Lambda$ is based on previous research [1]. The solution scheme is straightforward: we use conditions at the end of each interface as initial conditions for the next interface.

## 3.2 Ray Analysis

In order to successfully implement the solution scheme in the case of ray analysis, we must obey Snell's law at each interface. Recall that the refractive index distribution in the $p$th segment of the PSW is given by

$$n^2_{PSW}(x,z) = \begin{cases} n^2(x); & (p-1)\,\Lambda \le z \le (DC+p-1)\,\Lambda \\ n_0^2; & (DC+p-1)\,\Lambda < z < p\Lambda. \end{cases}$$

Snell's Law says that $n_1 \sin\theta_1 = n_2 \sin\theta_2$. In the case of the PSW, we may write, for $i \ge 2$ that

$$\theta_i = \begin{cases} \sin^{-1}\left(\frac{n(x_{i-1})}{n_0}\sin\theta_{i-1}\right), & i\ even \\ \sin^{-1}\left(\frac{n_0}{n(x_{i-1})}\sin\theta_{i-1}\right), & i\ odd \end{cases}$$

inside the waveguide. Here $x_i$ is the $x$-position at each of the $i$ interfaces, and the even $i$'s correspond to the high-low interfaces. The paraxial Hamiltonian equations of motion are solved in the high region, and the value of $\theta(d)$ is used to transfter the ray's slope between interfaces. The ray is a straight line in the low-index regions, since the equation of motion is a homogeneous second-order ODE without first or zero-eth order terms, i.e. $\ddot{x} = 0$. This line takes the form

$$x_{low}(z) = x_{high}(d) + (z-d)\theta_{new}, \tag{3.1}$$

where $\theta_{new}$ is the angle given by Snell's Law at the high-low interface. We expect to maintain the dynamical equilibria points at $x = 1 \pm \mu$ and $x = 1$, due to the persistence of equilibria [4]. Ray paths in the PSW are given in the next section.

### 3.2.1 Ray Paths

Simulations were ran with $P$=10 segments in the PSW, and $z \in [0, P\Lambda]$. Plots are shown in figure (3.1). Most configurations were found to guide the ray for input values of $x_0 = 1$ and

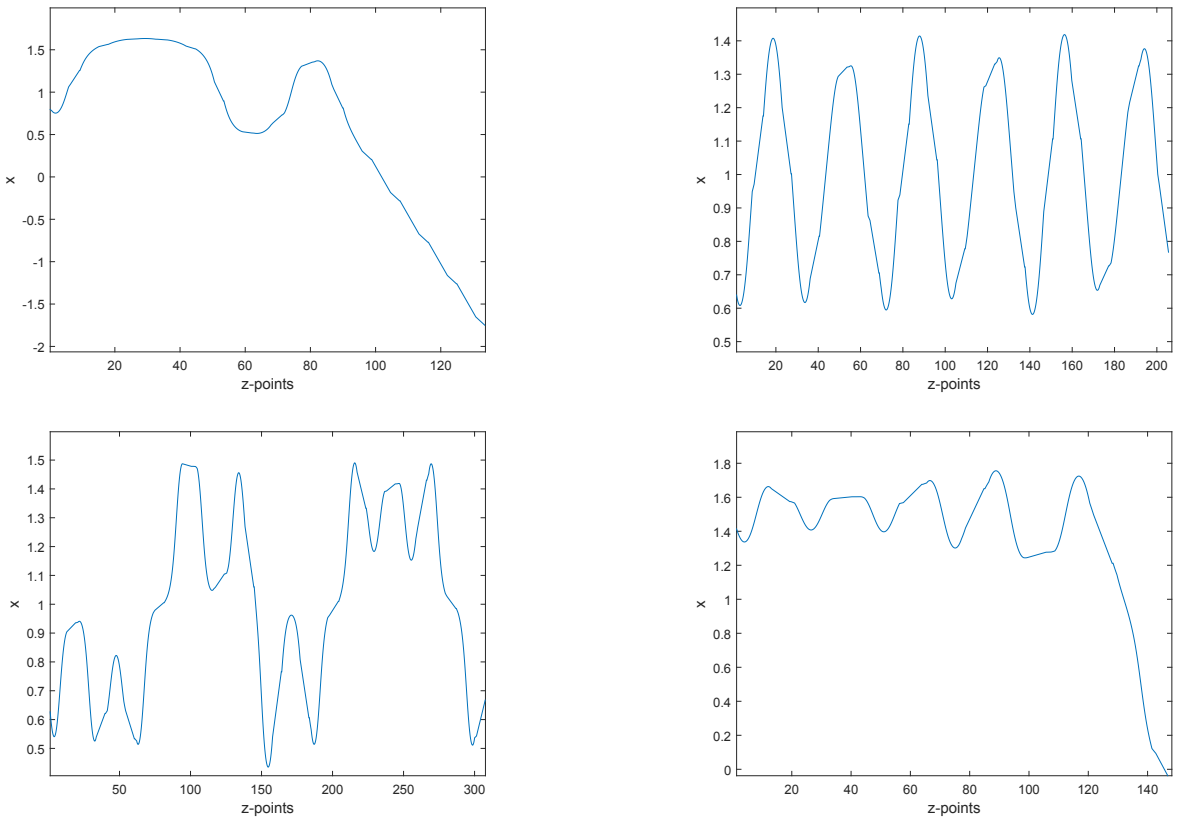


Figure 3.1: Paraxial ray trajectories in the PSW, for $\mu$= 0, .2, .3, and .5 (going left to right, row by row). $x_0$ was chosen to be just outside an equilibrium point and $\theta_0 = -\frac{\pi}{90}$. 120 "$z$-points" corresponds to a length of 1.2mm.

$\theta_0 = -\frac{\pi}{90}$. The configurations which eventually lost the light were when $\mu = 0$ and .5. The ray is guided for a small portion down the waveguide, but is dramatically kicked out passed a certain point. Explaining this behavior by looking solely at individual ray paths can be cumbersome. However, one may turn to phase space to get a better feel for the dynamics, and hopefully an explanation to this phenomenon.

### 3.2.2 Phase Space

The advantage of using a phase space formalism is that one may look at their configuration space and understand a great deal about the system of interest. A Poincaré section is a mapping

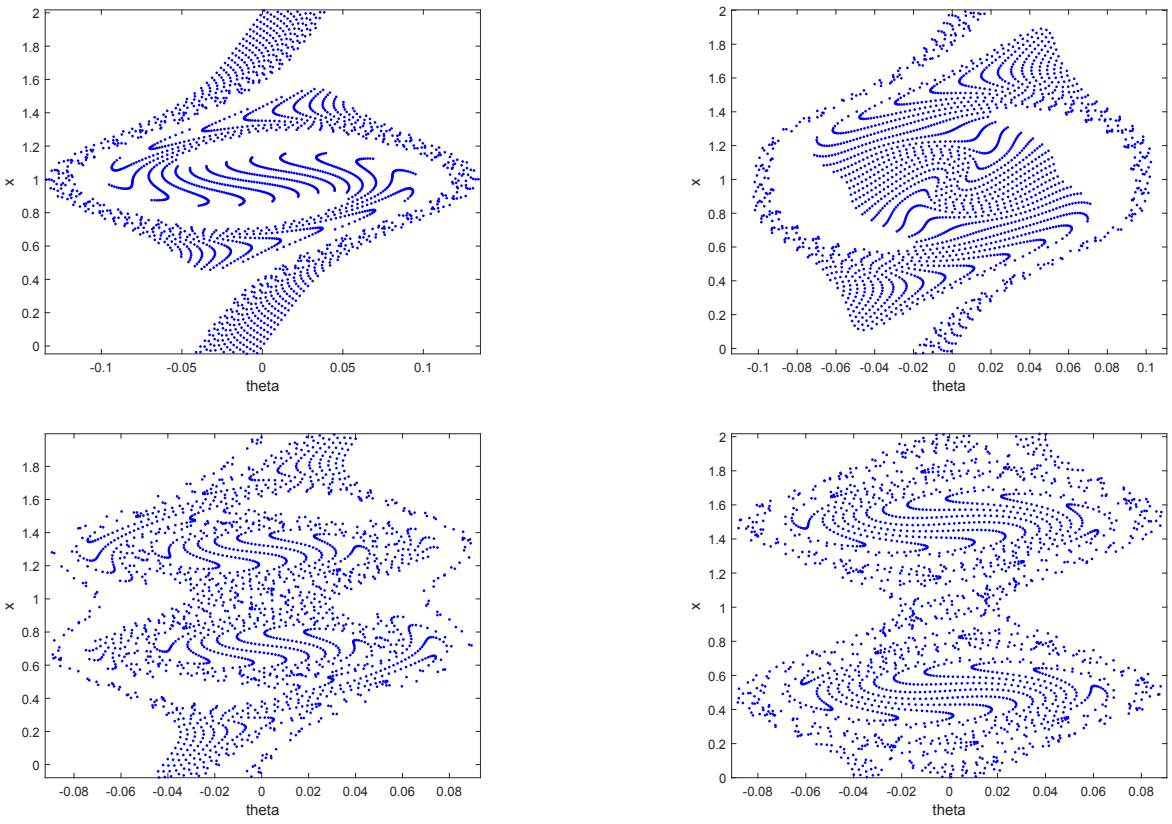


Figure 3.2: Stroboscopic plots of paraxial ray trajectories in phase space in the PSW, for $\mu$= 0, .2, .3, and .5 (going left to right, row by row). The regions of no discernible pattern are referred to as *Stochastic regions*, and correspond to regions of instability in the PSW.

from configuration space to $\mathbb{R}^2$ which captures a snapshot of the dyamics in the system. Akin to a Poincaré section, a stroboscopic plot is a picture of phase space which is periodic in time. Both reveal the underlying structure of the phase space in question. Since the Hamiltonian is periodic in $z$—which has been serving as the time variable—we seek to construct a stroboscopic plot of the phase space of the PSW. To accomplish such a task, simulations were run for 30 different $x_0$'s distributed evenly along $[0, 2]$ with an incident angle of $\theta_0 = -\frac{\pi}{90}$. Then trajectories $(x(z), \theta(z))$ were plotted whenever $z = n\Lambda$.

Another type of plot which would be handy for visualizing phase space is a parametric plot. These plots are built by simply ploting the solutions the equations of motion in phase space. Parametric plots were built for 100 different initial conditions and four segments. See figure (3.3).

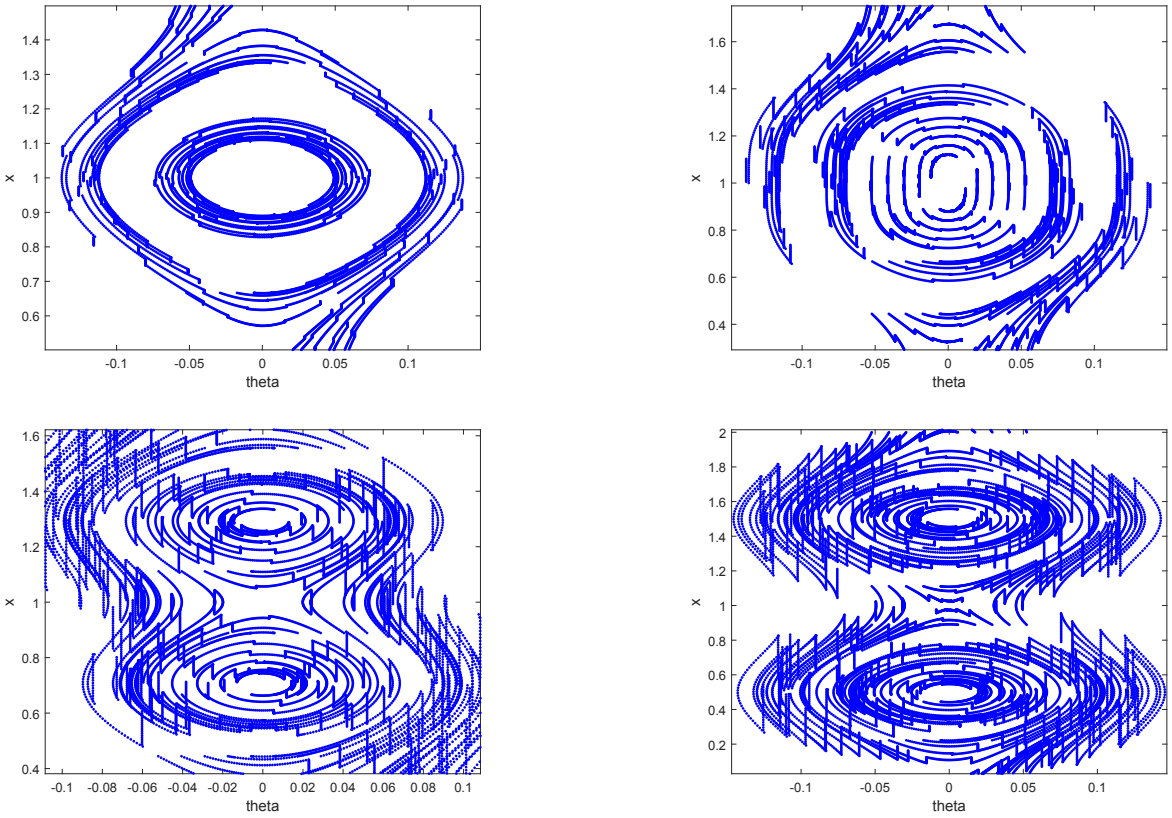


Figure 3.3: Parametric plots of paraxial ray trajectories in phase space in the PSW, for $\mu$= 0, .2, .3, and .5 (going left to right, row by row). The vertical lines are from the time/length the rays spend in the low index region, at constant slope.

While the structure of the visualizations in figures (3.2) and (3.3) is rather beautiful, we must remark they are expected. This is mostly by virtue of the nature of Hamiltonian systems (i.e. the dynamics take place on constant energy contours). Based on the plots in figure (3.2), we infer that the perturbation brought on by segmentation was small enough to ensure continued existence of the invariant Kolmogorov-Arnold-Moser (KAM) tori in phase space [4]. The centers of the tori are located at $x = 1 \pm \mu$.

The KAM tori represent loci of stable manifolds. There are lines of constant $\theta$ in phase space which seem to allow the rays to not be bound to level curves of constant energy. The trailing trajectories around the stable region signify a leaked ray. We thus arrive at an explanation for the phenonemenon observed in the figure (3.1): for $\mu$=.5, the initial conditions $x_0 = 1$ and $\theta_0 = -\frac{\pi}{90}$

are not close enough to a stable resonance in phase space, and thus the ray gets kicked out of the waveguide as a result of interaction with the saddle equilibrium at $x = 1$.

The structure of phase space as revealed by the stroboscopic and parametric plots signals the existence of *wave chaos* in the PSW. To understand more about the PSW, we turn to the wave picture.

## 3.3 Wave Analysis

We seek the solution to the parabolic wave equation:

$$\frac{i}{k_0}\partial_z\psi = H_{opt}\psi,$$

where $H_{opt} = T + V_{opt}$ is the paraxial optical Hamiltonian, defined as

$$H_{opt} = \frac{\nabla_t^2}{2n_0k_0^2} + \frac{n^2(\mathbf{r}, z) - n_0^2}{2n_0}.$$

For the case of one transverse dimension, the parabolic wave equation becomes

$$\frac{i}{k_0}\partial_z\psi(x, z) = \frac{\partial_x^2\psi(x, z)}{2n_0k_0^2} + V_{opt}(x, z)\psi(x, z). \tag{3.2}$$

### 3.3.1 Analytic Solution in Low-Index Regions

In this section, we solve the parabolic wave equation with respect to zero Dirichlet boundary condtions and some initial profile $\psi_0(x) = \psi(x, z = 0)$ for $x \in [0, L]$. In the low-index regions, we have that $n^2(\mathbf{r}, z) = n_0^2$. This zeroes out the potential term and the parabolic wave equation reduces to

$$\frac{i}{k_0}\partial_z\psi(x, z) = \frac{\partial_x^2\psi(x, z)}{2n_0k_0^2}.$$

$$\implies \partial_z\psi(x, z) = \alpha\partial_x^2\psi(x, z),$$

where $\alpha = \frac{-i}{2n_0k_0}$. In this way, the parabolic wave equation is mathematically equivalent to the diffusion equation, with an imaginary diffusion constant. Since the solution to the diffusion equation

on $[0, L]$ with zero Dirichlet boundary conditions is well-defined, we may write the solution to the parabolic wave equation explicitly:

$$\psi(x, z) = \int_0^L dy\ \psi_0(y) G(x, y, z), \tag{3.3}$$

where $G(x, y, z)$ is the *Green's Function* of the diffusion equation on a finite domain:

$$G(x, y, z) = \frac{2}{L} \sum_{n=1}^{\infty} \sin(\lambda_n x) \sin(\lambda_n y) e^{-\alpha \lambda_n^2 z} \tag{3.4}$$

$$= \frac{2}{L} \sum_{n=1}^{\infty} \sin\left(\frac{n\pi x}{L}\right) \sin\left(\frac{n\pi y}{L}\right) \exp\left(\frac{i n^2 \pi^2 z}{2 n_0 k_0 L^2}\right), \tag{3.5}$$

which can be found using separation of variables [43]. Since we also know that

$$\psi(x, z) = \sum_{n=1}^{\infty} \langle \phi_n(x), \psi_0(x) \rangle \phi_n(x) e^{-i k_0 \varepsilon_n z},$$

(the $n = 0$ term is identically zero) we can solve for the eigenvalues of the Hamiltonian in the low index regions:

$$-i k_0 \varepsilon_n = \frac{i n^2 \pi^2}{2 n_0 k_0 L^2}$$

$$\implies \varepsilon_n = -\frac{n^2 \pi^2}{2 n_0 k_0^2 L^2},\ n \in \mathbb{N}.$$

The optical Hamiltonian is thus negative definite in the low-index regions. We note that the eigenvalues, probably unsurprisingly, are similar in form to the energy levels of an electron wave function in an infinite square well.

We expect to maintain the low-order error in implementing this method with the strategy used for continuous waveguides. This means that there will be error propagation through the PSW simulations, as the initial condition at each interface will have this order of error associated with it.

### 3.3.2 Results

Simulations were ran on an $x$-grid of 512 points, and evaluated for ten segments. Paraxial propagation of light in the PSW is shown in figure (3.4). $x_0$ was chosen to vary with the value of

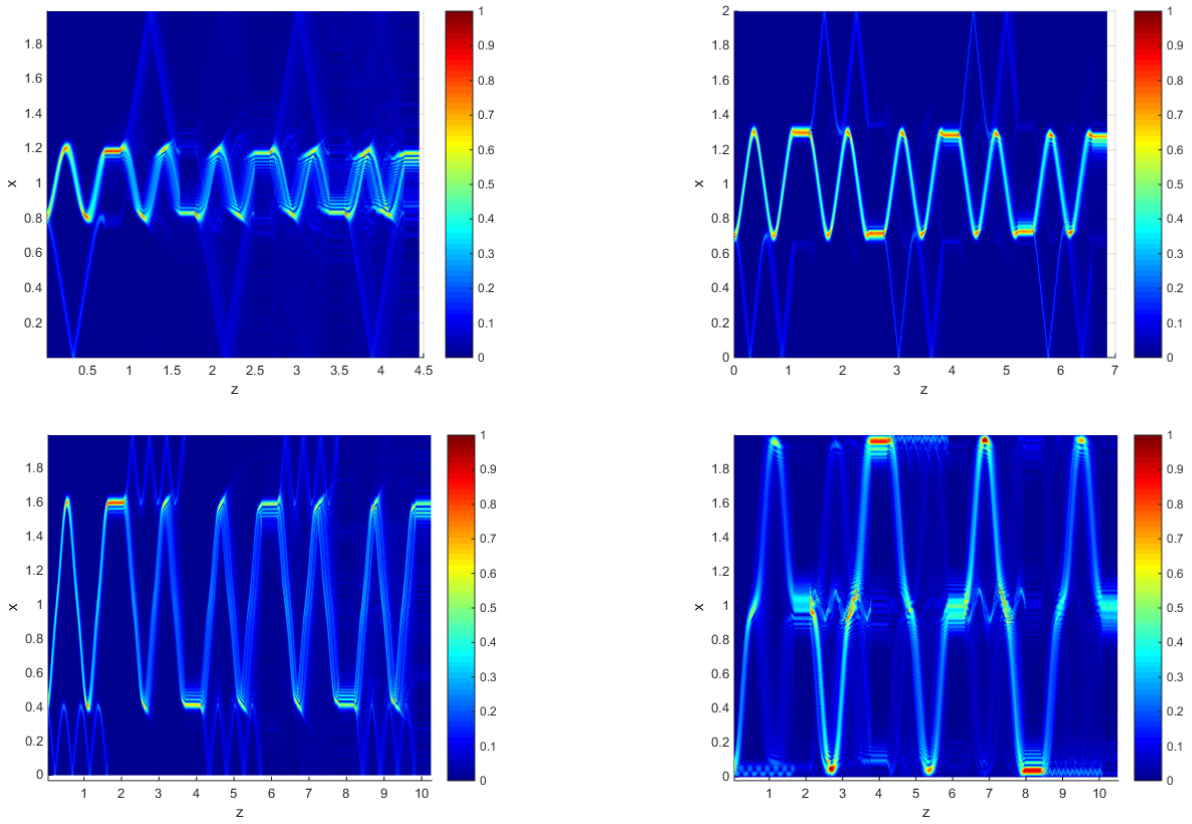


Figure 3.4: Contour plots of Paraxial propagation in the PSW, for $\mu$= 0, .2, .3, and .5 (going left to right, row by row). Here $x_0$ varies based on the value of $\mu$ and $\theta_0 = 0$. Artifacts are standing waves generated by the Dirichlet boundary conditions.

$\mu$, while $\theta_0 = 0$. For all values of $\mu$, the light is seen to propagate in an approximately sinusoidal fashion down the PSW. This complex behavior might be explained by way of analogy to the ray analysis. That is, light stays guided due to interactions with dynamical resonances within the PSW. This assertion might be backed by the plotting of a *Husimi Distribution*, which is the wave-analysis counterpart to a Poincaré section [1].

Modal power spectra were also calculated in all of these cases, and a spectrua of the PSW (for all cases of $\mu$) can be found in figure (3.5). The thickness of the spectra near the end indicates a plethora of nearly-degenerate guided modes which have a slow variation in the group delay of the modes [42]. It is interesting to take note of the spike in the later part of the spectrum. This spike means that some of the higher-order modes contain a noticible part of the power within the PSW.

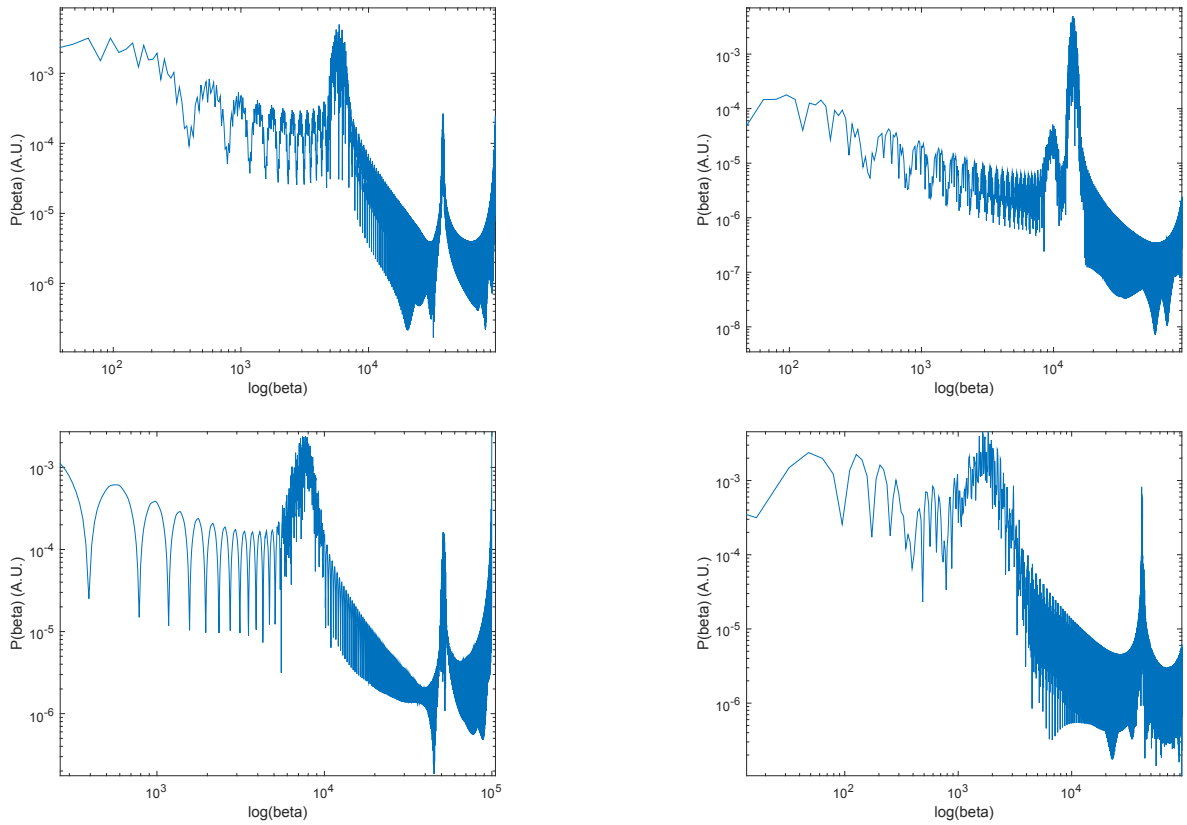


Figure 3.5: Typical modal power spectrum in thePSW, for $\mu$= 0, .2, .3, and .5 (going left to right, row by row).

The spike happens because the high degree of degeneracy between the higher-order modes, which creates a resonance. This resonance is existent due to the interaction with the separatrix in the geometry of the high-index regions.

# Chapter 4

# Further Considerations

In this chapter we offer concluding remarks on the analysis presented herein. Variation of parameters is performed to arrive at an integral expression for the parabolic wave equation on a finite domain with zero Dirichlet boundary conditions. Then a full spectral method is briefly described. The chapter ends with some final thoughts.

## 4.1 Alternate Solution Methods

Here we consider the case of non-zero, $z$-varying optical potential. To set up the analysis, recall that the solution to the parabolic wave equation on a finite domain with zero Dirichlet boundary condi tions can be written as

$$\psi(x,z) = \sum_{n=0}^{\infty} b_n(z) \sin(\lambda_n x), \tag{4.1}$$

where $\lambda_n = \frac{n\pi}{L}$. In this case, we write the 1-D parabolic wave equation in the following form:

$$\left(\frac{i}{k_0}\partial_z - \frac{\partial_x^2}{2n_0k_0^2}\right)\psi(x,z) = V_{opt}(x,z)\psi(x,z). \tag{4.2}$$

We are concerned with the solution to this equation for $x \in [0,L]$ subject to zero Dirichlet boundary conditions and some initial condition $\psi_(x, z=0) = \psi_0(x)$. We note that we may expand the right-hand side in a Fourier series:

$$V_{opt}(x,z)\psi(x,z) = \sum_{n=0}^{\infty} f_n(z) \sin(\lambda_n x), \tag{4.3}$$

where

$$f_n(z) = \frac{2}{L}\int_0^L V_{opt}(x,z)\psi(x,z)\sin(\lambda_n x)\,dx. \tag{4.4}$$

### 4.1.1 Analytic

Plugging equations (4.1) and (4.3) into equation (4.2), we arrive at an ODE for the $z$-dependent expansion coefficients:

$$b_n'(z) + \alpha\lambda_n^2 b_n(z) = -ik_0 f_n(z), \tag{4.5}$$

where $\alpha = \frac{-i}{2n_0k_0}$. This can be solved with an integration factor to obtain

$$b_n(z) = \left(b_0 - ik_0\int_0^z f_n(s)e^{\alpha\lambda_n^2 s}ds\right)e^{-\alpha\lambda_n^2 z}. \tag{4.6}$$

We can then use initial condition $\psi_0$ in conjunction with the definition of $f_n(z)$ to write

$$b_n(z) = \frac{2}{L}\int_0^L dy\ \left(\psi_0(y) - ik_0\int_0^z V(y,s)\psi(y,s)e^{\alpha\lambda_n^2 s}ds\right)\sin(\lambda_n y)e^{-\alpha\lambda_n^2 z}. \tag{4.7}$$

Or, in a more compact form

$$b_n(z) = \frac{2}{L}\int_0^L dy\ F(y,z)\sin(\lambda_n y)e^{-\alpha\lambda_n^2 z}. \tag{4.8}$$

Thus the implicit solution $\psi(x,z)$ is

$$\psi(x,z) = \sum_{n=0}^{\infty}\frac{2}{L}\int_0^L dy\ F(y,z)\sin(\lambda_n x)\sin(\lambda_n y)e^{-\alpha\lambda_n^2 z} \tag{4.9}$$

$$= \int_0^L dy\ F(y,z)G(x,y,z), \tag{4.10}$$

where $G(x,y,z)$ is the Green's Function as defined in equation (3.5).We finally see that the parabolic wave equation can be expressed as a set of coupled integral equations:

$$\psi(x,z) = \int_0^L dy\ F(y,z)G(x,y,z), \tag{4.11}$$

$$F(y,z) = \psi_0(y) - ik_0\int_0^z V(y,s)\psi(y,s)e^{\alpha\lambda_n^2 s}ds \tag{4.12}$$

It is interesting to note that (4.11) is of the form of a Fredholm equation of the first kind, and, when plugged into (4.12), a Fredholm equation of the second kind arises. Subsequently performing a back-substitution yields the first-order approximation of the *Born Series*:

$$\psi(x,z) = \int_0^L dy \ \left(\psi_0(y) - ik_0 \int_0^z ds \int_0^L dy \ F(y,s)N(y,s)e^{\alpha\lambda_n^2 s}\right) G(x,y,z), \tag{4.13}$$

where $N(y,s) = G(y,y,s)V(y,s)$. This approximation is used in atomic scattering problems [44]. One might imagine that this could be useful in the theoretical study of PSWs in interferometry.

### 4.1.2 Numerical

An alternative to the preceeding analysis is to note that, equation (4.6) is a convolution expression:

$$b_n(z) = b_0 e^{-\alpha\lambda_n^2 z} - ik_0 \left(f_n(z) * e^{-\alpha\lambda_n^2 z}\right), \tag{4.14}$$

and thus the Born Series can be calculated numerically by iterating vectors corresponding to the sine transform of the product $V_{opt}(x,z)\psi_0(x)$ through this equation and summing subsesequent iterations. It may be ill-advised to attempt to calculate the series to a large number of terms when the potential term is large, however, since the series grows in powers of $G(y,y,s)V(y,s)$!

In addition the spectral methods used and mentioned in this thesis, methods such as Crank-Nicholson discretization and Multigrid methods can be used (even in conjunction) to dramatically reduce the error incurred in numerical simulations.

## 4.2 Conclusions

A qualitative study of the ray and wave dynamics of light in slab waveguides, whose transverse index profile is similar to that of the effective index profile of the dual tapering waveguide (DTW), has been presented. Two types of slab waveguides were studied: a continuous guide and a Periodically Segmented Waveguide. Both waveguides were seen to exhibit interesting guidance properties which were reliant on the large number of modes within the guide.

The Periodically Segmented Waveguide showcased notable guidance behavior. The PSW

performed similar to its continuous counterpart, with the added bonus of intensifying the input signal due to segmentation. Results were given for PSWs with varying duty cycle and a segmentation period of $2\mu$m. In the ray picture, it was shown that invariant KAM tori in phase space are essentially preserved under the small perturbation performed in this thesis. The preservation of these tori lead to the guidance of rays. Rays which were not close enough to one of these tori initially were eventually leaked out of the wave guide. Stroboscopic and parametric plots of phase space confirming this assertion were constructed.

In the wave treatment of the PSWs, the calculated modal power spectrum offers a means of interpretation as to the modal properties of the PSW. The areas of thickness in the spectrum correspond to a large number of degenerate modes. The presence of these areas indicate the region in the spectrum whose values are close to the energy of the separatrix present in the optical potential. The degeneracy in this region is so dramatic that it causes a resonance in the later end of the spectrum.

The results presented in this thesis seem to imply that—to low order (because of the numerical error)—the quantum separatrix crossing theory outlined in [5] is valid for small, discontinuous, nonautonomous perturbations in the potential. One might surmise that the theory should be valid for perturbations smaller than the wavelength of light used in the waveguide regardless of the perturbation's continuity. However, this is mere speculation.

The first aspect of this analysis to address is the accuracy of the solution method. The easiest way to improve the results herein would be to substitute the use of the composite Simpson's rule with a discrete sine transform of the initial condition. A more modern, sophisticated numerical method could in principle drive the accuracy down to an arbitrarily small order. This would allow for a finer resolution of the solution, and thus may reveal more interesting properties concerning the erratic nature of the dynamics associated with the PSW. A coupled mode analysis and asymptotic methods have the potential to produce analytic results which could also in principle be implemented to high order. We further note that the PSW is similar to a periodic crystaline structure, so a Bloch modal ansatz for the electric field would be appropriate to analyze the PSW [31]. A loss analysis is

warranted to investigate the applicability and practicality of waveguides with separatrix geometry. Finally, it would be of great interest to study the behavior of PSWs with circular cross-sections.

We conclude that light travels in a sinusoidal fashion in the continuous slab waveguide with a tranverse refractive index profile similar to the effective index of the DTW. The guide is multimoded with nearly degenerate higher-order modes present in the spectrum contributing to the optical power in the slab. Upon the introduction of discontinuous periodic perturbations along the optical axis, the segmented waveguide guides light through the interactions of the degenerate higher-order modes within the guide. The multitude of these modes signal the breakdown of the adiabatic parameter in the waveguide, but did not exhibit mode trapping for any of the initial conditions used.

## Bibliography


[1] P. Aschiéri and V. Doya, "Snake-like light beam propagation in multimode periodic segmented waveguide," vol. 30, no. 12, pp. 3161–3167, 2013.

[2] C. Michel, S. Tascu, V. Doya, P. Aschiéri, W. Blanc, O. Legrand, and F. Mortessagne, "Experimental phase-space-based optical amplification of scar modes," Physical Review E - Statistical, Nonlinear, and Soft Matter Physics, vol. 85, pp. 5–8, 2012.

[3] V. Doya, O. Legrand, C. Michel, and F. Mortessagne, "Scar Selection in an Optical Fibre," vol. 112, no. 4, pp. 607–617, 2007.

[4] J. Meiss, Differential Dynamical Systems. SIAM, 2007.

[5] J. R. Cary and P. Rusu, "Quantum Dynamics Near a Classical Separatrix," vol. 47, no. 4, pp. 2496–2505, 1993.

[6] A. Snyder and J. D. Love, Optical Waveguide Theory. Chapman and Hall, 1983.

[7] I. Januar, "Characteristics of Integrated Optical Devices and Structures." Guided Wave Optics Laboratory, 1992.

[8] D. D. Holm, "Geometric Mechanics Part I: Dynamics and Symmetry," vol. 1, p. 468, 2011.

[9] J. Synge, Geometrical Optics. Cambridge University Press, 2008. 3rd printing.

[10] O. D. Enersen, "Thomas Young." `http://www.whonamedit.com/doctor.cfm/1715.html`, 2015. Accessed: 2015-02-13.

[11] C. Pask, "Mathematics and the science of analogies," American Journal of Physics, vol. 71, no. 2003, p. 526, 2003.

[12] G. Elert, "Photoelectric effect." `http://physics.info/photoelectric/`, 2015. Accessed: 2015-02-13.

[13] G. Agrawal, "Nonlinear fiber optics: its history and recent progress," Josa B, vol. 28, no. 12, pp. 0–1, 2011.

[14] V. Alwayn, "A brief history of fiber-optic communications." `http://www.ciscopress.com/articles/article.asp?p=170740`, 2015. Accessed: 2015-02-13.

[15] D. Marcuse, Theory of Dielectric Waveguides. Academic Press, 1991.

[16] K. F. Barrell and C. Pask, "Ray launching and observation in graded-index optical fibers," Journal of the Optical Society of America, vol. 69, no. 2, p. 294, 1979.

[17] A. W. Snyder, D. J. Mitchell, and C. Pask, "Failure of geometric optics for analysis of circular optical fibers," Journal of the Optical Society of America, vol. 64, no. 5, p. 608, 1974.

[18] a. W. Snyder and C. Pask, "Geometric optics limit of Marcuse's coupled power equations.," Applied optics, vol. 15, no. 4, pp. 868–869, 1976.

[19] A. Ankiewicz and C. Pask, "Potential Symmetry in Dynamics and the Onset of Chaos," vol. 101, no. 5, pp. 239–245, 1984.

[20] A. Torre, Linear Ray and Wave Optics in Phase Space. Elsevier, 2005.

[21] D. D. Holm and G. Kovačič, "Homoclinic chaos for ray optics in a fiber," Physica D: Nonlinear Phenomena, vol. 51, pp. 177–188, 1991.

[22] A. Ghatak, Optics. Tata McGraw-Hill, 2009. 2nd printing.

[23] A. Mickelson, Physical Optics. Van Nostrand Reinhold, 1992.

[24] D. Nir, Z. Weissman, S. Ruschin, and a. Hardy, "Periodically segmented waveguides in Ti:LiNbO(3).," Optics letters, vol. 19, no. 21, pp. 1732–1734, 1994.

[25] Z. Weissman and a. Hardy, "Modes of periodically segmented waveguides," Journal of Lightwave Technology, vol. 11, no. 11, pp. 1831–1838, 1993.

[26] J. Amin, J. a. Aust, and N. a. Sanford, "Z-propagating waveguide lasers in rare-earth-doped Ti:LiNbO3," Applied Physics Letters, vol. 69, p. 3785, 1996.

[27] V. Rastogi, a. K. Ghatak, D. B. Ostrowsky, K. Thyagarajan, and M. R. Shenoy, "Ray analysis of parabolic-index segmented planar waveguides.," Applied optics, vol. 37, no. 21, pp. 4851–4856, 1998.

[28] P. Aschiéri, V. Rastogi, L. Chanvillard, P. Baldi, M. P. De Micheli, D. B. Ostrowsky, G. Bellanca, P. Bassi, K. Thyagarajan, and M. R. Shenoy, "Experimental observation of longitudinal modulation of mode fields in periodically segmented waveguides.," Applied optics, vol. 38, pp. 5734–5737, 1999.

[29] P. Aschiéri, V. Doya, and A. Picozzi, "Complex behaviour of a ray in a Gaussian index profile periodically segmented waveguide," Journal of Optics A: Pure and Applied Optics, vol. 8, pp. 386–390, 2006.

[30] "Ray dispersion strongly modified by a periodic index segmentation," Optics Communications, vol. 283, no. 19, pp. 3673–3677, 2010.

[31] P. Aschiéri and V. Doya, "Unexpected light behaviour in periodic segmented waveguides," Chaos, vol. 21, 2011.

[32] A. Julia, R. F. Oliveira, M. S. Costa, C. E. Rubio-Mercedes, V. F. Rodriguez-Esquerre, and O. Member, "Numerical Analysis of Periodic Segmented Waveguides Directional Couplers," 2012.

[33] C. E. Rubio-Mercedes, V. F. Rodriguez-Esquerre, I. T. Lima, and H. E. Hernandez-Figueroa, "Analysis of straight periodic segmented waveguide using the 2-D finite element method," Journal of Lightwave Technology, 2014.

[34] A. Bange, H. B. Halsall, and W. R. Heineman, "Microfluidic immunosensor systems," Biosensors and Bioelectronics, vol. 20, pp. 2488–2503, 2005.

[35] L. Chrostowski and D. Ratner, "Improving the performance of silicon photonic disks, rings, and Bragg gratings for use in label-free biosensing," vol. 9166, pp. 1–38.

[36] A. G. Markelz, J. R. Knab, J.-Y. Chen, J. Cerne, and W. a. Cox, "Tagless and universal biosensor for point detection of pathogens," vol. 5411, pp. 182–186, 2004.

[37] K. P. Zetie, S. F. Adams, and R. M. Tocknell, "How does a Mach-Zehnder interferometer work?," Physics Education, vol. 35, no. January, pp. 46–48, 2000.

[38] R. Nave, "Fabry-Perot Interferometer." `http://hyperphysics.phy-astr.gsu.edu/hbase/phyopt/fabry.html`, 2015. Accessed: 2015-03-15.

[39] N. Kinrot, "Analysis of bulk material sensing using a periodically segmented waveguide Mach-Zehnder interferometer for biosensing," Journal of Lightwave Technology, vol. 22, no. 10, pp. 2296–2301, 2004.

[40] N. Kinrot and M. Nathan, "Investigation of a periodically segmented waveguide Fabry-P??rot interferometer for use as a chemical/biosensor," Journal of Lightwave Technology, vol. 24, no. 5, pp. 2139–2145, 2006.

[41] K. Atkinson, An Introduction to Numerical Analysis. Wiley, 1988.

[42] "Computation of mode eigenfunctions in graded-index optical fibers by the propagating beam method.," Applied optics, vol. 19, pp. 2240–2246, 1980.

[43] Guenther and Lee, Partial Differential Equations of Mathematical Physics and Integral Equations. Prentice Hall, 1998.

[44] D. Griffiths, Introduction to Quantum Mechanics. Pearson, 2004.